

CHARACTERIZATION AND FABRICATION
OF
SILICON THIN FILMS FOR SOLAR CELL APPLICATIONS

A THESIS SUBMITTED TO
THE GRADUATE SCHOOL OF NATURAL AND APPLIED SCIENCES
OF
MIDDLE EAST TECHNICAL UNIVERSITY

BY
MEHMET KARAMAN

IN PARTIAL FULFILLMENT OF THE REQUIREMENTS
FOR
THE DEGREE OF MASTER OF SCIENCE
IN
MICRO AND NANOTECHNOLOGY

AUGUST 2011

Approval of the Thesis:

CHARACTERIZATION AND FABRICATION OF SILICON THIN FILMS FOR SOLAR CELL APPLICATIONS

Submitted by **MEHMET KARAMAN** in partial fulfillment of the requirements
for the degree of **Master of Science in Micro and Nanotechnology**
Department, Middle East Technical University, by,

Prof. Dr. Canan Özgen
Dean, Graduate School of **Natural and Applied Sciences** -----

Prof. Dr. Mürvet Volkan
Head of Department, **Micro and Nanotechnology** -----

Prof. Dr. Raşit Turan
Supervisor, **Physics Dept., METU** -----

Assist. Prof. Dr. H. Emrah Ünalan
Co-Supervisor, **Metallurgical and Materials Eng., METU** -----

Examining Committee Members:

Prof. Dr. Macit Özenbaş
Metallurgical and Materials Engineering Dept., METU -----

Prof. Dr. Raşit Turan
Physics Dept, METU -----

Prof. Dr. Çiğdem Erçelebi
Physics Dept, METU -----

Assist. Prof. Dr. H. Emrah Ünalan
Metallurgical and Materials Engineering Dept, METU -----

Assist. Prof. Dr. Özge Tüzün Özmen
Physics Dept., Düzce University -----

Date : 25.08.2011

I hereby declare that all information in this document has been obtained and presented in accordance with academic rules and ethical conduct. I also declare that, as required by these rules and conduct, I have fully cited and referenced all material and results that are not original to this work.

Name, Last Name : Mehmet Karaman

Signature : 

ABSTRACT

CHARACTERIZATION AND FABRICATION OF SILICON THIN FILMS FOR SOLAR CELL APPLICATIONS

Karaman, Mehmet

M. Sc. Department of Micro and Nanotechnology

Supervisor : Prof. Dr. Raşit Turan

Co-Supervisor : Assist. Prof. Dr. H. Emrah Ünalan

August 2011, 78 pages

In this thesis study, fabrication and characterization of silicon thin films prepared by magnetron sputtering and electron beam evaporation for solar cell applications have been investigated. In the first part of the study, magnetron sputtering method was used to fabricate thin hydrogenated amorphous silicon (a-Si:H) film on a Si substrate. Some samples were prepared on glass substrate for the basic characterizations like transmission and resistivity. Dark and illuminated I-V characteristics of the silicon heterojunction (SHJ) solar cells were studied as a function of material type and process parameters. It was observed that devices show diode characteristics, however their response to the illumination was quite weak. Low performance of the devices was discussed in terms of the resistivity and dopability of the sputtered film. The second part of the thesis deals with the fabrication and characterization of thin polysilicon films fabricated by e-beam evaporation. In order to dope the deposited Si films, a very thin boron film

was deposited by e-beam evaporation on SiO_2 surface thermally grown on a Si wafer. Then an a-Si was evaporated by the same technique. Samples were annealed for polysilicon formation by using the technique called solid phase crystallization (SPC). The annealing was performed in two steps. The first step was the nucleation part, carried out at 475°C for 8 hours and the second step was the diffusion and crystallization parts that are accomplished at 900°C for several minutes. The Raman measurements revealed out the crystallinity and grain size. The crystallinity of the polysilicon thin films was also identified by X-Ray diffraction measurements. Finally, the Secondary Ion Mass Spectroscopy (SIMS) analysis was carried out to find out the amount of boron that diffuses into Si film. It was found that a graded boron profile, which is desirable for the solar cell applications, was achieved.

Keywords: Amorphous silicon, SPC

ÖZ

GÜNEŞ GÖZELERİ UYGULAMALARI İÇİN SİLİSYUM İNCE FILMLERİN ÜRETİM VE KARAKTERİZASYONLARI

Karaman, Mehmet

Yüksek Lisans, Mikro ve Nanoteknoloj Bölümü

Tez Yöneticisi : Prof. Dr. Raşit Turan

Ortak Tez Yöneticisi : Yrd. Doç. Dr. H. Emrah Ünalan

Ağustos 2011, 78 sayfa

Bu tez çalışmasında magnetron saçtırma ve elektron demeti buharlaşturma yöntemleriyle üretilen silisyum ince filmlerin karakterizasyonları ve güneş pili uygulamaları çalışılmıştır. Çalışmanın ilk bölümünde, c-Si alttaş üzerine üretilen ince amorf silisyum (a-Si:H) için magnetron saçtırma yöntemi kullanılmıştır. Bazı örnekler geçirgenlik ve özdirenç ölçümü gibi temel karakterizasyon yöntemleri için cam alttaş üzerine üretilmiştir. Değişik malzeme yapısı ve deney parametreleri bakımından karanlıkta ve ışık altındaki I-V özelliklerini çalışılmıştır. Aygıtların, diyon karakteristiği göstermesine rağmen ışık altındaki tepkisi oldukça az olduğu gözlemlenmiştir. Bu sonuçlar, filmlerin özdirenç ve katkılabilirliği açısından tartışılmıştır. Tezin ikinci bölümünde e-demeti yöntemiyle üretilmiş olan polisilisyum ince filmler ele alınmıştır. Silisyum filmleri katkılayabilmek için ısisal yöntemle üretilmiş SiO_2 kaplı silisyum dilim üzerine e-demeti yöntemiyle ince boron film üretilmiştir. Daha sonra aynı yöntemle amorf silisyum üretimi yapımıştir. Amorf silisyumu polisilisyuma çevirmek için katı faz kristalleşmesi (SPC) yöntemi kullanılarak örnekler fırınlanmıştır. Fırınlama iki aşamada gerçekleşmiştir. İlk aşama çekirdeklenme bölümü olup

475°C'de 8 saat, ikinci aşama ise difüzyon ve kristalizasyon bölümü olup 900°C'de değişik dakikalarda yapılmıştır. Değişik sürelerde fırınlanmış örneklerin Raman ölçümleri tanelerin kristallliğini göstermiştir. Polisilisyum ince filmlerin kristalliği aynı zamanda X-Işını kırınımı ölçümleriyle de belirlenmiştir. Son olarak, polisilisyum içine boron difüzyonunu tayin etmek için ikincil iyon kütlesi spektroskopisi (SIMS) analizi yapılmıştır. Güneş pili uygulaması için uygun olan kademeli B profilinin üretildiği gözlemlenmiştir.

Anahtar kelimeler: Amorf silisyum, SPC

To my family

ACKNOWLEDGEMENTS

I would like to thank Professor Raşit Turan for his support, instructive discussions, introducing the facilities during my M.Sc education and thesis work. Also I would like to thank Assist. Prof. Dr. Emrah Ünalan for his cooperation in studies. I am thankful to Assist. Prof. Dr. Özge Tüzün Özmen for adapting her experience and instructive comments during the thesis work. Thanks to Mustafa Kulakçı for sharing his knowledge and experience. Thanks to Zeynep Deniz Eygi for her informations about the study. I would also like to thank Professor Mehmet Parlak, Tahir Çolakoğlu, Olgun Demircioğlu, Zeynep Türkşen Demircioğlu, Fırat Es, Ersan Harputlu, Kutlu Kutluer, Seda Kayra Güllü, Hasan Hüseyin Güllü, Yücel Eke, Serim İlday, Hakan Karaağaç, İrem Tanyeli, Makbule Bilgen, Erdem Katı, Banu Kosif, all Semiconductor Materials Devices and Solar Energy group for their support and friendship.

I am thankful to my colleagues and the staff in Atilim University Physics Group for their support and understanding.

I am also thankful to my family for their support and confidence throughout my life.

TABLE OF CONTENTS

ABSTRACT.....	iv
ÖZ.....	vi
ACKNOWLEDGEMENTS	viii
TABLE OF CONTENTS.....	x
LIST OF TABLES.....	xiii
LIST OF FIGURES	xiv
CHAPTERS	
1. INTRODUCTION	1
1.1. Solar Energy	1
1.1.1. Solar Energy And The Market.....	1
1.1.2. Solar Radiation	2
1.2. Photovoltaic Conversion	4
1.2.1. Basics of Photovoltaic Effect.....	4
1.2.2. Photovoltaic Cell Parameters.....	6
1.3. Silicon Photovoltaic Technologies.....	11
1.3.1. Monocrystalline and Polycrystalline Solar Cells	11
1.3.2. Amorphous and Microcrystalline Thin Film Solar Cells	12
1.3.3. Thin Film Polycrystalline Silicon Solar Cells	14
1.3.4. Silicon Heterojunction (SHJ) Solar Cells	16
2. FABRICATION OF Si THIN FILMS FOR PHOTOVOLTAIC APPLICATONS.....	19
2.1. Fabrication of Silicon Heterojunction Solar Cells	19
2.1.1. Deposition of Amorphous Silicon by Sputtering	19

2.1.2. The Sputtering System	21
2.1.3. The Samples.....	22
2.2. Fabrication of Polycrystalline Si Thin Films.....	24
2.2.1. Deposition of Thin Si Film by e-Beam Evaporation.....	24
2.2.2. The E-Beam System.....	26
2.2.3. Sample Preparation	26
2.3. The Measurement System.....	28
3. USE OF Si THIN FILM FABRICATED BY MAGNETRON SPUTTERING FOR HETEROJUNCTION SOLAR CELL	32
3.1. Basic Device Structure.....	32
3.2. Amorphous Silicon	37
3.3. SHJ Solar Cells fabricated by magnetron sputtering.....	40
3.3.1. Effect of the sputter type	45
3.3.2. Effect of sputtering power	47
3.3.3. Effect of substrate type	48
3.4. Discussion on the use of Si thin film fabricated by magnetron sputtering	50
4. POLYCRYSTALLINE SILICON THIN FILMS AND SOLAR CELL APPLICATIONS.....	53
4.1. Electronic Properties of Polycrystalline Materials and Electronic Transport.....	53
4.2. Polycrystalline Silicon Thin Films: Fabrication and Characterization.....	58
4.2.1. Raman Analysis	59
4.2.2. XRD Results	65
5. CONCLUSIONS.....	70

BIBLIOGRAPHY	75
--------------------	----

LIST OF TABLES

TABLES

Table 1: Some important results of SHJ solar cells.....	17
Table 2: a-Si:H thin films prepared by magnetron sputtering	24
Table 3: Annealing durations for the samples	28
Table 4: p-1 and p-2 samples	42
Table 5: Process parameters of samples p-3, p-4, p-5 and n-1	44
Table 6: Solar cell characteristics of the samples	50
Table 7: Some example resistance values	51
Table 8: Crystalline fractions of the samples obtained from Raman measurements	64

LIST OF FIGURES

FIGURES

Figure 1: Global photovoltaic installation forecast.....	2
Figure 2: Solar radiation spectrum and effect of atmosphere	3
Figure 3: Air Mass concept	3
Figure 4: a) Absorbing the light, b) Excitation to CB, c) Charge separation .	5
Figure 5: (a) p-type, (b) n-type materials and (c) p-n junction	6
Figure 6: Schematic view of a p-n junction solar cell	7
Figure 7: Dark I-V graph of (a) ,pn junction, (b) illuminated pn junction	8
Figure 8: Solar cell I-V curve.....	9
Figure 9: Solar cell operating parameters	10
Figure 10. Monocrystalline (left) and polycrystalline (right) silicon solar cells	12
Figure 11: (a) Single junction amorphous and micromorph solar cell, (b) spectral response of micromorph solar cell.....	13
Figure 12: Thin film Polysilicon solar cell	15
Figure 13: Schematic view of SHJ solar cell	16
Figure 14: (a) Schematic view of sputtering process and (b) sputter deposition chamber.....	20
Figure 15: Schematic of the sputtering system used in this work.....	22
Figure 16: Schematic of a typical evaporation system	25
Figure 17: Schematic of E-beam evaporation System	26

Figure 18: I-V measurement set-up	28
Figure 19: Schematic of X-Ray Diffraction	30
Figure 20: n-type and p-type semiconductors having different bandgaps	33
Figure 21: Band bending following contact formation of two semiconductors	33
Figure 22: Depletion region on both sides of the junction	35
Figure 23: Trap states at the interface an electron hole motion	36
Figure 24 : Amorphous silicon structure and possible coordination of atoms	37
Figure 25: PDF of crystalline and amorphous solid and gas	38
Figure 26: Density of states of amorphous silicon.....	39
Figure 27: Effect of hydrogenation	40
Figure 28:Tauc plot for bandgap as-grown and hydrogenated a-Si	41
Figure 29: Dark I-V measurements of p-1 and p-2.....	43
Figure 30: Illuminated I-V measurements of samples p-1 and p-2.....	43
Figure 31: A picture of the sample with the solar cell grids	45
Figure 32: Dark and illuminated I-V measurements of samples p-3 and p-4	46
Figure 33: Solar simulator I-V measurement of p-3 and p-4	47
Figure 34: Dark and illuminated results of sample p-5	48
Figure 35: Dark and illuminated results of sample n-1	49
Figure 36: Solar Simulator results of samples n-1 and p-5	49
Figure 37: Ideal heterojunction band diagram.....	51
Figure 38: Heterojunction with impeded carrier motion.....	51
Figure 39: Schematic of polycrystalline silicon film	53
Figure 40: The effect of dangling bonds and defects	54

Figure 41: Polycrystalline silicon with low dopant concentration	56
Figure 42: Polycrystalline silicon with increased dopant concentration.....	56
Figure 43:Polycrystalline silicon following the filling of trap states	57
Figure 44: Schematic view of the sample before and after annealing	58
Figure 45: Raman spectra of sample A, annealed at only at 475°C/8h.....	60
Figure 46: Raman spectra of sample B.....	61
Figure 47: Raman spectra of sample C and D	62
Figure 48: Raman spectra of samples D, E and A	63
Figure 49: Raman spectra of samples A, D and E at low wavenumbers	63
Figure 50: Peak Fit analysis for Sample C	65
Figure 51: X-Ray diffraction spectra of sample A.....	66
Figure 52: X-Ray diffraction spectra of sample B.....	66
Figure 53: X-Ray diffraction spectra of sample C.....	67
Figure 54: X-Ray diffraction spectra of sample D.....	67
Figure 55: SIMS profile of sample C	68
Figure 56: SIMS profile of sample D	68

CHAPTER 1

INTRODUCTION

1.1. Solar Energy

1.1.1. Solar Energy And The Market

The detriment of increasing carbon dioxide in the atmosphere has reached a huge amount up to now and creatures start to get their portion from this effect. The greenhouse gases are giving permanent impacts to the environment and affects the human life as shortening of food, water and energy. The new energy sources other than fossil fuels are needed for human being to live in healthy environment without any threat for their future.

Another reason for the search of new energy resources is the shortening of fossil fuels. Day to day, the energy demand of the world increases with the rising population. According to the American Energy Information Administration (EIA), energy consumption will be nearly doubled in 2040 [1]. This situation inspires people to use the renewable energy sources more efficiently and encourage the researchers to improve the present technologies. Major renewable sources are the solar energy, wind power, wave power, biomass, hydro power, and geothermal. Among these, solar energy is the most abundant one that can supply the energy needed by the world's population. It has also an advantage for isolated places to where they are away from the grid. Electricity from sun has no damage to environment since there is no toxicity and waste products. It can be categorized as the cleanest and most abundant source of energy.

Photovoltaic energy conversion is one of the major technologies of solar energy conversion. The history of the photovoltaic technologies started with the discovery of photovoltaic effect by Becquerel in 1839. Russell Ohl owned the first patented modern semiconductor solar cells in 1946 [2]. The highly efficient solar cell was first developed by Daryl Chapin, Calvin Sauthier Fuller and Gerald Pearson in 1954 using a diffused silicon p-n junction [3]. For the last 30 years, photovoltaics has recorded remarkable progress and today Gigawatt solar power installations have been reached (Figure 1).

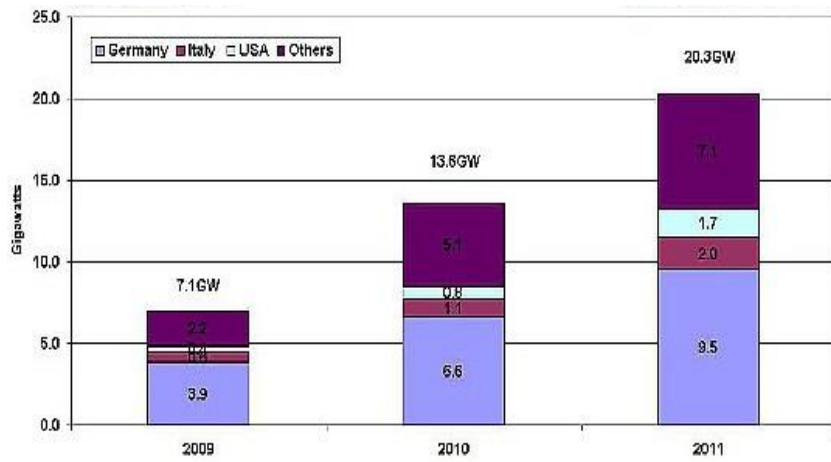


Figure 1: Global photovoltaic installation forecast [4]

1.1.2. Solar Radiation

Sun, as an energy source, delivers 1.2×10^{14} kW energy to the earth and this is 10000 times greater than the present energy demand [5]. When the sun light reaches the atmosphere only a portion of radiation is absorbed by the earth. Some of the radiation is absorbed by the atmosphere and some reflected back to the space. Solar radiation spectrum describes the effect of atmosphere on wavelength and intensity (Figure 2). The temperature on the surface of the sun is about 6000K, which behaves like a blackbody radiation source. As a result, the spectrum on the surface of atmosphere is similar to a

blackbody which has a surface temperature of 6000K. The radiation intensity just above the Earth's atmosphere is about 1350 W/m^2 [6]. When the light passes through the atmosphere, intensity decreases depending on the distance travelled. The air mass concept takes the effect of atmosphere on the intensity into account.

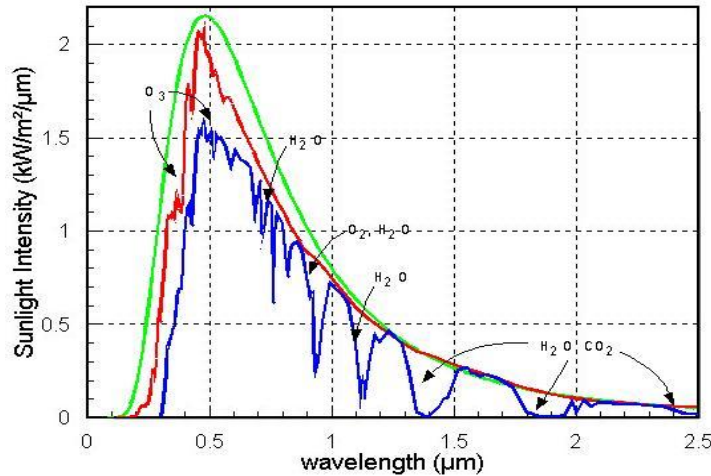


Figure 2: Solar radiation spectrum and effect of atmosphere [7]

Simple schematic view of Air Mass concept is shown in Figure 3.

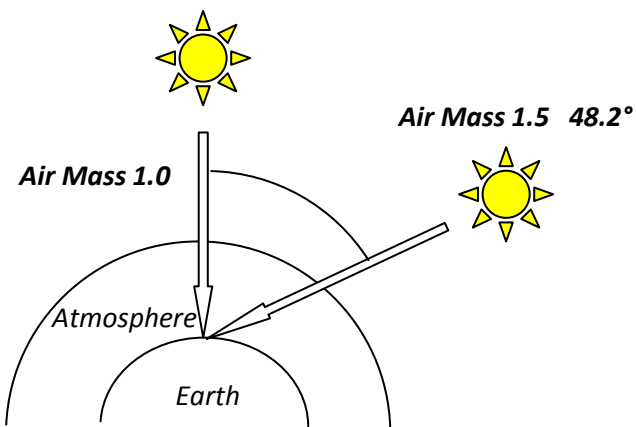


Figure 3: Air Mass concept

This concept is simply expressed by the equation;

$$\text{Air Mass} = 1 / \cos(\theta) \quad (1)$$

where θ is the angle of incidence. Air mass is the measure of absorption through the optical path in the atmosphere. When the sun is just ahead, the power on the sea level is determined by the air mass one radiation (AM 1). In Figure 2 the red line represents the AM 0 and blue line represents AM 1.5 conditions and Air mass 0 states the power on the surface of atmosphere which is 1353 W/m^2 . A standard for solar cell test measurements is done under AM 1.5 condition where θ corresponds to 48.2° [8]. This thickness of atmosphere result in a radiation power around 1000 W/m^2 on the sea level. Wavelengths below $0.3 \mu\text{m}$ are filtered by oxygen ozone and nitrogen, however, H_2O and CO_2 causes significant absorption in the infrared region as shown in Figure 2.

1.2. Photovoltaic Conversion

1.2.1. Basics of Photovoltaic Effect

Solar photovoltaic energy conversion is based on the conversion of light energy into the electrical energy. The light is composed of quantized energy packets called photons, whose energy is stated by the frequency or color of the light and given by

$$E(eV) = h\nu = \frac{1240}{\lambda(nm)} \quad (2)$$

where h is the Planck's constant, ν is the frequency and λ is the wavelength of light. To obtain an electrical energy, one needs the flow of free electrons and holes created by the light energy. In a photovoltaic device, the electrons absorb the energy of photons and are excited to the conduction band, where they are nearly free to move (Figure 4). However, the created electrons and

holes tend to relax back to their original position which is called recombination. A charge separation and transport mechanism are then necessary, to create an electrical current . This is only possible if there exist a built-in potential asymmetry to force electrons and holes to move toward the external contacts (Figure 4)

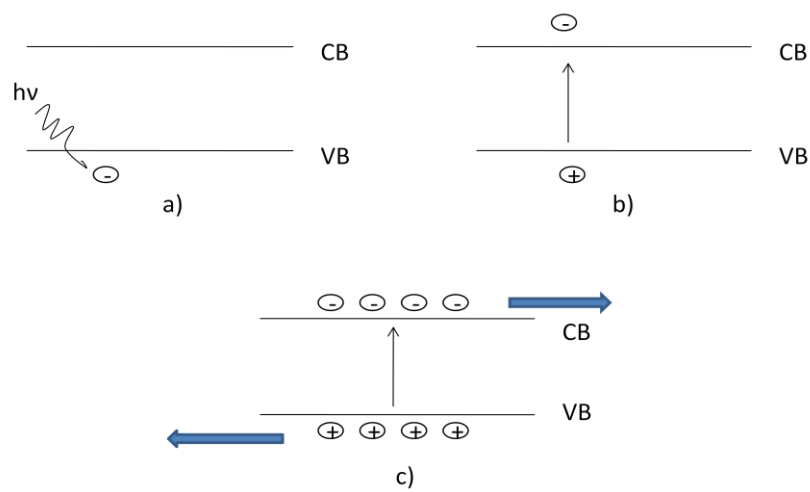


Figure 4: a) Absorbing the light, b) Excitation to CB, c) Charge separation

In a semiconductor device this asymmetry is created by a junction between two electronically different materials. In a so-called p-n junction, electric field is formed by a dipole system as a result of charge transfer and Fermi level alignment.

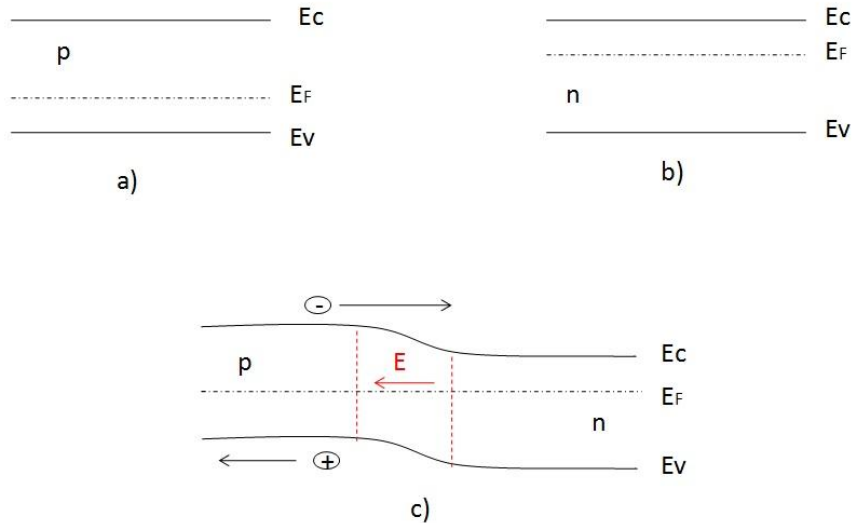


Figure 5: (a) p-type, (b) n-type materials and (c) p-n junction

In Figure 5, separately p and n type materials and schematic representation of a p-n junction is given. When p and n type materials contact each other, majority electrons start to diffuse from n to p region and majority holes move from p region to n region. This diffusion continues until the electric field formed at the junction reaches a high enough value, so that it does not permit any further flow of carriers. This electric field separates the holes and electrons in the photovoltaic action.

1.2.2. Photovoltaic Cell Parameters

Schematic of the cross section of a p-n junction solar cell is shown in Figure 6.

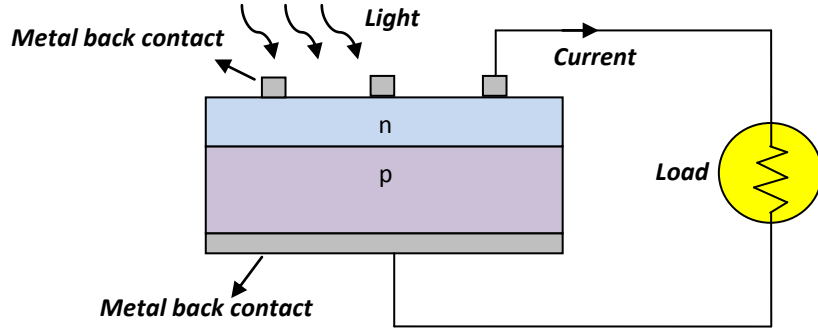


Figure 6: Schematic view of a p-n junction solar cell

p-n junction of solar cell also behaves like an ordinary diode when the device is measured in the dark with the typical diode equation of

$$I = I_0 \left(e^{\frac{q(V_0-V)}{kT}} - 1 \right) \quad (3)$$

where I_0 is the dark saturation current which is constant and I is the current flowing through the device when the V is applied to the contacts on the p and n type regions. q is the electric charge, k is the Boltzmann constant, V_0 is the built-in potential determined by the doping concentrations and T is the absolute temperature. Without illumination when the device is forward biased the majority carriers in n-type (electrons) start to flow, by the reduction of barrier, to the p-type region. Holes have the opposite movement. If the device is illuminated, the dark saturation current which is formed by the minority carriers, (electrons in p-type, holes in n-type region) will increase because the carriers are excited by the light energy. If the contribution from light energy is added to equation (3), then

$$I = I_0 \left(e^{\frac{qV}{kT}} - 1 \right) + I_L \quad (4)$$

I_L is the current generated by the light which is in the opposite direction with the forward biased current. The current-voltage (I-V) characteristics of a p-n junction in dark and under illumination are shown in Figure 7. The overall effect of the illumination is to shift the curve in the negative direction of the current axis. For the solar cell analysis, the fourth quadrant of the I-V curve (positive V , negative I) is studied

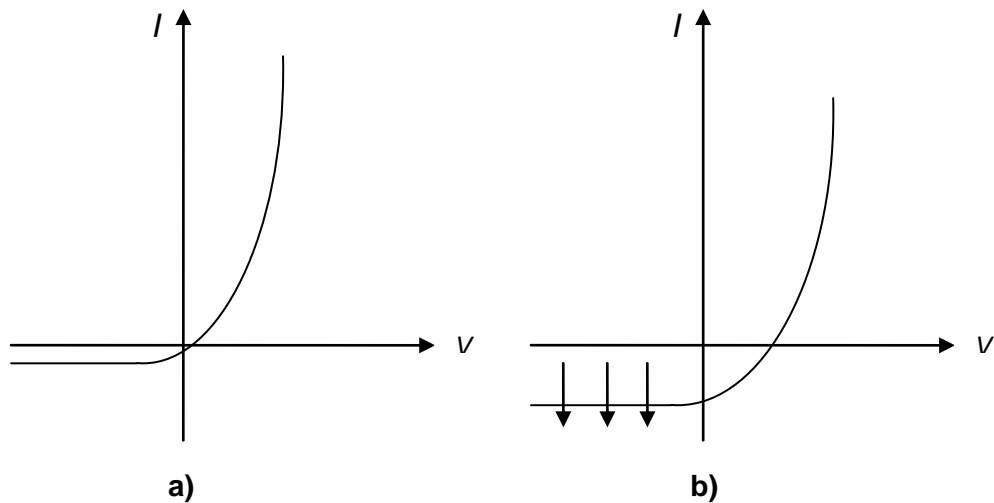


Figure 7: Dark I-V graph of (a) ,pn junction, (b) illuminated pn junction

However, mirrored demonstration of this quadrant is used for the convenience as shown in Figure 8.

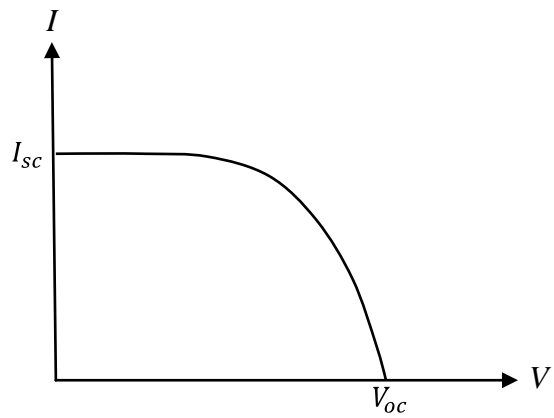


Figure 8: Solar cell I-V curve

Short circuit current; when there is no net voltage across the terminals of the solar cell the current flowing is the short circuit current (I_{sc}), or in other words, the current flowing when there is no external load in the circuit. The carrier generation and collection are the main parameters that identify short circuit current. Therefore, light intensity, cell area, reflectance and collection probability are the subparameters of carrier generation and all affect the amount of short circuit current.

Open circuit voltage; when the terminals of the cell is isolated from each other, the cell produces a voltage between terminals under illumination. This is called open circuit voltage (V_{oc}). Open circuit voltage is determined by the band gap of the material and the built-in potential generated by the p-n junction.

Series resistance; series resistance is caused by several mechanisms. First of all, the carriers move through the cell material, between emitter(n) and base(p), which means through a resistive material. Another resistance creating part is the contact resistance between silicon and metal, which is needed for external connections. In addition to these, resistance of the back and front metal contacts themselves which contribute to series resistance. The series resistance reduces the fill factor and if it exceeds certain level the short circuit current decreases too. The series resistance is represented as the inverse slope of I-V curve near open circuit voltage;

$$R_s = \left. \frac{1}{\frac{dI}{dV}} \right|_{V=V_{oc}} \quad (5)$$

Shunt resistance; The shunt resistance is a measure of short circuit across the p-n junction. It is usually caused by the manufacturing defects which forms easy conduction channel through the p-n junction. It determines the leakage of current across the junction and must be high for an ideal solar cell. Shunt resistance is shown as the inverse slope of the I-V curve around the short circuit current

$$R_{sh} = \left. \frac{1}{\frac{dI}{dV}} \right|_{V=0} \quad (6)$$

Fill factor; Fill factor defines the maximum power that can be extracted from a solar cell. It is defined as the ratio of the extractable power to $V_{oc} \times I_{sc}$. This is equivalent to the ratio of two rectangles shown in Figure 9. The inner rectangle in Figure 9 is given by I_{max} and V_{max} . The outer rectangle corresponds to the total maximum power that can be extracted from an ideal solar cell with no series resistance and infinite shunt resistance. The fill factor increase with decreasing series resistance and increasing shunt resistance

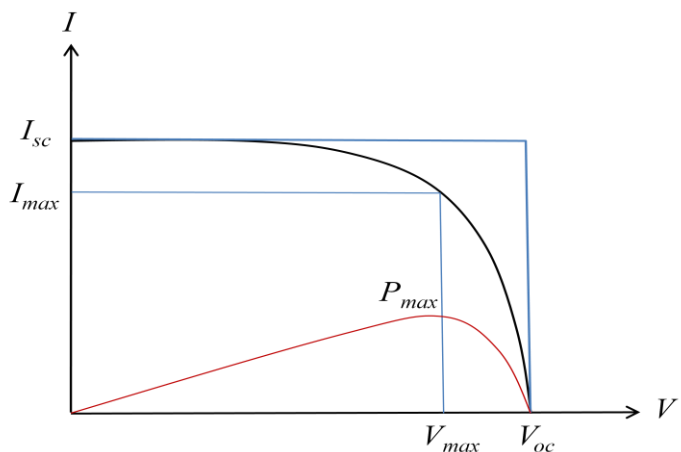


Figure 9: Solar cell operating parameters

$$FF = \frac{V_{max} I_{max}}{V_{oc} I_{sc}} \quad (7)$$

Efficiency; The efficiency of a solar cell is perhaps the most important parameter of a solar cell. It simply compares the input solar power and output electrical power extracted from the cell. The efficiency of a solar cell is commonly given using a standard solar radiation that has been accepted as a general reference for the solar cell evaluation. This standard is called AM1.5 condition which is approximately equal to 1000 W/m². Mathematically the efficiency is defined as;

$$\eta = \frac{P_{out}}{P_{in}} = \frac{V_{max} I_{max}}{1000 \frac{W}{m^2} X Area} \quad (8)$$

The solar cell efficiencies quoted refers to this definition.

1.3. Silicon Photovoltaic Technologies

1.3.1. Monocrystalline and Polycrystalline Solar Cells

Monocrystalline and polycrystalline solar cells are historically first solar cells developed in 1960s. They are usually considered as the first generation solar cell. In spite of their relatively high cost, these type of solar cells, as the most mature and reliable technology, dominates the solar cell market today. Typical mono and multicrystalline solar cell devices are shown on Figure 10

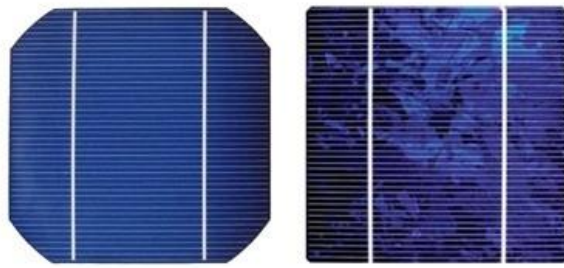


Figure 10. Monocrystalline (left) and polycrystalline (right) silicon solar cells [9]

The crystalline Si solar cells stems from the fact that the material and device has reached very high quality as a result of extensive research efforts carried out in the last 50 years. In addition, the active part of the device, i.e., the p-n junction, is formed by deriving the doping front into the pure crystalline substrate. This makes the the p-n junction free from any contamination that might naturally exists at artificially formed interfaces.

The major disadvantage of the crystalline cells is the high cost due to the extensive material usage. Module efficiencies about 19% have been reached with monocrystalline silicon solar cell. However, for the polycrystalline silicon, the module efficiency about 17% has been achieved [10]. Different cell and contact designs are still under investigation to push the efficiency to higher values.

1.3.2. Amorphous and Microcrystalline Thin Film Solar Cells

An amorphous silicon solar cell consisting of thin a-Si layers in the form of p-i-n structure as shown in Figure 10. It is the most mature thin film photovoltaic technology today, referred to as the second generation solar cell. Low cost and relatively easy production technology have attracted many researchers to work on amorphous silicon (a-Si:H). This has led to a significant market share in the PV market in the last 30-35 years. The most important advantages of a-Si:H solar cell is that it can be fabricated at low

temperatures ($<300^{\circ}\text{C}$) on different substrates like glass, metals, flexible materials. a-Si:H can be deposited either by physical vapor deposition (PVD) like e-beam evaporation, sputtering or chemical vapor deposition (CVD) like plasma enhanced chemical vapor deposition (PECVD), hot wire chemical vapor deposition (HWCVD) techniques. The most widely used PV technology is the PECVD technique. Since a-Si:H has higher absorption coefficient than c-Si, less than 500nm of thickness is enough to construct a solar cell, hence, only less than 1% of silicon used in c-Si solar cells is sufficient for the fabrication of a solar cell. Recently 9.5 % efficiency has been obtained in a single junction a-Si:H p-i-n solar cell [11]. Although the efficiency value is almost half of that of c-Si solar cells the cost of the generated energy is comparable to the c-Si solar cells due to the low production cost. The market share of the thin film solar cells is expected to increase in the coming years.

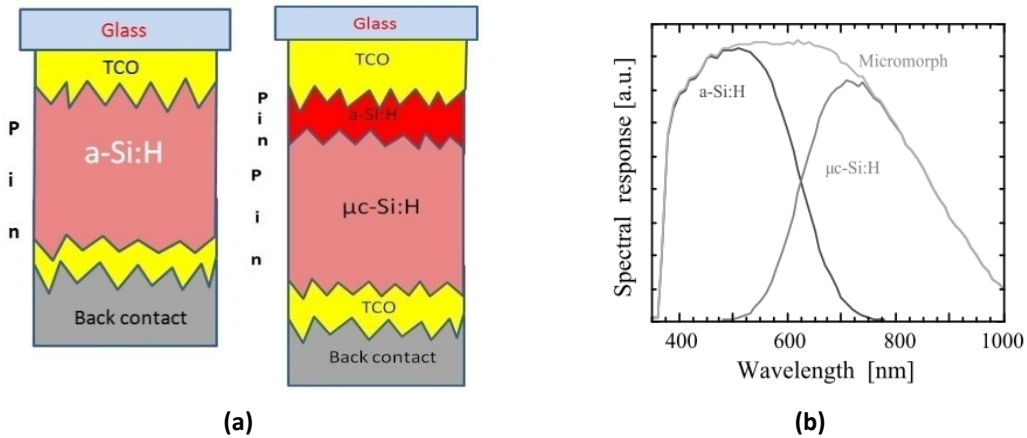


Figure 11: (a) Single junction amorphous and micromorph solar cell, (b) spectral response of micromorph solar cell [12]

Micromorph solar cell concept has been developed to improve the sensitivity of the device by allowing absorption from a wider solar spectrum. A typical micromorph solar cell has two p-i-n structures stacked as shown in Figure 11. Two junctions consisting of an a-Si:H p-i-n structure as the top cell and microcrystalline silicon ($\mu\text{c-Si:H}$) p-i-n as the bottom cell, cover two different

regions of the solar spectrum, and hence improve the efficiency. These two p-i-n devices complement each other to give a wider response to solar radiation (Figure 11b). a-Si:H, has a bandgap of 1.7eV and absorbs high energy photons while μ c-Si:H has the properties of c-Si with a bandgap of 1.12 eV; so μ c-Si:H cell undertakes the task of absorbing infrared region. The well known solar cell equipment manufacturer, Oerlikon has recently achieved the stabilized efficiency of 11.9% in micromorph solar cells [13]

1.3.3. Thin Film Polycrystalline Silicon Solar Cells

Thin film crystalline silicon solar cell studies appeared in literature in 1990s. In general, this concept aims to combine the advantages of crystalline and thin film Si in the same cell structure. As a thin film structure it uses less material than c-Si solar cell, while as a crystalline Si, it has higher performance like c-Si solar cell in terms of the efficiency. However, it is a challenging task to fabricate thin film crystalline solar cells as described below. The thickness of the Si layer used in these solar cells is around 1-2 μ m in a device structure shown in Figure 12. It is important to note that the amount of material is 100-200 times less than c-Si solar cells. Here the technique used is called Solid Phase Crystallization (SPC), where thin film amorphous silicon is transformed into polycrystalline silicon structure by applying a special annealing procedure. In a polycrystalline material, electronic transport is affected by the grain boundaries which act as the carrier scattering centers. For this reason, it is desirable to have as large grains as possible for improved electron and hole transport. Since the crystallization starts at temperatures above 600°C, substrates used must withstand to those temperatures such as refractory materials like quartz, borosilicate glass, or stainless steel. a-Si can be deposited by PECVD, HW-CVD, e-beam evaporation. Among these techniques, e-beam evaporation has the advantage of high rates up to 1 μ m/min [14] and does not include toxic and flammable gases like silane. In order to keep the growth

temperature as small as possible, the SPC growth has been employed for very long times up to 20 hours at 600°C [15].

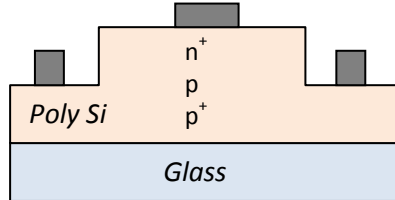


Figure 12: Thin film Polysilicon solar cell

First significant development on thin film c-Si solar cells was reported by Sanyo Electric before mid 1990s. The solar cell they fabricated was a 5 μm thick PECVD deposited silicon on metal substrate. Crystallization was done at 600°C and an efficiency of 9.2% was obtained [16]. In late 1990s Pacific Solar in Australia deposited silicon layer on borosilicate glass and developed solutions for light trapping [17] and metallization [18] in the following years. As a result, they fabricated solar cell with a film thickness of 2.2 μm giving an efficiency of 10.4% with an area of 94 cm^2 , a *FF* of 72.1%, J_{sc} of 29.5 mA/cm^2 and V_{oc} of 492 mV. In 2004, the licence for crystalline silicon on glass (CSG) was acquired and the company called CSG Solar AG was founded in Germany. Silicon depositon was transferred to large area glass of 1.4 m^2 and in 2007 the module efficiency of 8% was accomplished [19]. Another considerable study on SPC was reported from the University of New South Wales(UNSW). A film thickness of 2-3 μm on textured glass was crystallized at 600°C, and generated an efficiency of 9%. The cell area of 4 cm^2 produced J_{sc} of 26 mA/cm^2 , V_{oc} of 500mV and *FF* of 70% [20].

1.3.4. Silicon Heterojunction (SHJ) Solar Cells

The concept of using amorphous silicon on c-Si to fabricate heterojunction solar cell dates back to 1970s. First a-Si/c-Si heterojunction diode, which was fabricated using evaporated intrinsic silicon on Si wafer was reported in 1968 [21]. However in those early years hydrogenated a-Si was not elaborated yet, and for this reason, the a-Si was too defective for an efficient solar cell device. In 1974 the first hydrogenated a-Si thin film with less defect structure was reported [22]. Today, heterojunction solar cell studies includes not only Si, but also other semiconductor and oxide materials like amorphous oxides, amorphous germanium and CdS. Following the success in substitutional doping of hydrogenated amorphous silicon by glow discharge technique [23], interest in photovoltaic applications of silicon heterostructures increased due to the potential of fabricating solar cells with efficiencies higher than the c-Si solar cells. First of all, SHJ solar cell production needs no complex techniques like oxidation. As shown in Figure 13 it has a simple structure. Furthermore, the process can be conducted at low temperatures ($<300^{\circ}\text{C}$) compared to furnace doping ($\sim 900^{\circ}\text{C}$) of crystalline wafers. The fundamental SHJ solar cell consists of a top n/p a-Si:H layer on p/n c-Si wafer (Figure 13).

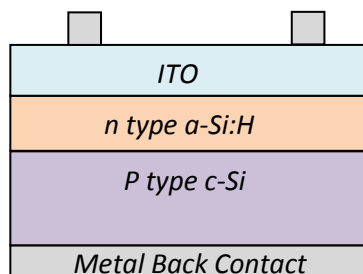


Figure 13: Schematic view of SHJ solar cell

In 1980s, SHJ of (n) a-Si:H / (p) poly-Si / was produced as low cost single junction solar cell [24]. The studies on SHJ solar cells continued on surface passivation mechanism to reduce the surface recombination effects. After an

extensive research and development study, SANYO announced first SHJ solar cell with an intrinsic amorphous layer between doped a-Si:H and c-Si. This new solar cell called heterojunction with an intrinsic thin layer (HIT), employs an intrinsic amorphous layer between p-type a-Si:H and n-type c-Si with an n-type a-Si:H back surface passivation. The efficiency of the first device was reported to be 13.6 % for a 100 cm² area [25]. Nowadays SANYO reported the record efficiency values around 23 % with HIT solar cell [26]. Different research centers and companies are carrying out research and development studies on SHJ solar cells. Table 1 summarizes the achievement reported from these studies.

Table 1: Some important results of SHJ solar cells

	FZ/CZ	Area (cm ²)	Jsc (mA/cm)	V _{oc} (mV)	FF (%)	η(%)
Sanyo	n CZ	100cm ²	39.5	729	80	23.0
NREL	p FZ	0.9	35.9	678	78.6	19.1
	n FZ	0.9	35.3	664	74.5	17.2
Helmholtz Centre Berlin	n FZ	1	39.3	639	79	19.8
	p FZ	1	36.8	634	79	18.5
IMT EPFL	n FZ	0.2	34	682	82	19.1
	p FZ	0.2	32	690	74	16.3

Magnetron sputtering is a commonly used technique to fabricate a-Si thin films. It is a low temperature process and can be preferred over the other techniques for device fabrication on substrates like glass and flexible counterparts. It is very suitable for large area deposition. The most important

advantage of the sputtering is that it does not employ any toxic and flammable material for the a-Si thin film deposition. However, no significant achievement has been reported for SHJ solar cells fabricated by magnetron sputtering. One of the aims of this study is to investigate the fabrication of a-Si thin films using magnetron sputtering.

CHAPTER 2

FABRICATION OF Si THIN FILMS FOR PHOTOVOLTAIC APPLICATIONS

2.1. Fabrication of Silicon Heterojunction Solar Cells

2.1.1. Deposition of Amorphous Silicon by Sputtering

Sputtering is a technique that atoms are ejected from a target material by highly energetic particles. It is generally used for surface cleaning and patterning of surfaces where microscale process is necessary [27]. Sputter deposition is the thin film deposition of sputtered atoms onto substrates. The physics behind sputtering is the momentum transfer between the energetic ions and source atoms as a result of collisions. Simply, after the evacuation of the chamber down to process pressures ($\sim 10^{-6}$, 10^{-7} Torr), the inert gas (generally Ar) is introduced into the chamber. Then, applying high voltage (target/cathode, substrate/anode) will arc the Ar atoms to the plasma state and excited Ar^+ ions will accelerate towards the negatively biased target. These high speed ions hit the target and sputter the source atoms. Sputtered atoms are spread around and they stick onto the substrate in the form of a thin film.

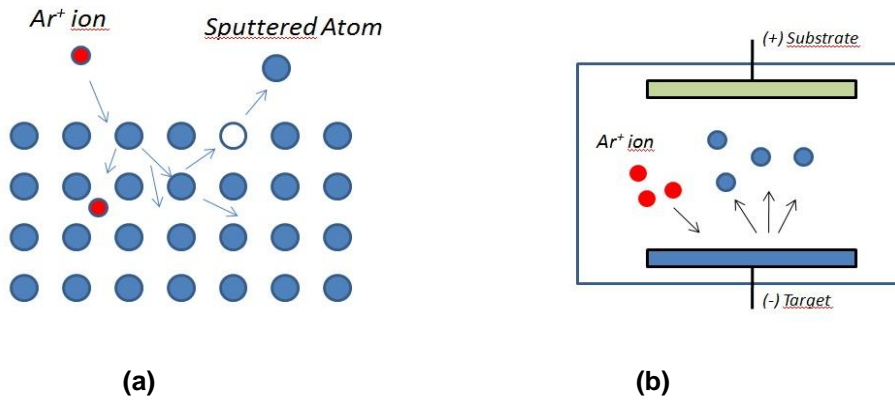


Figure 14: (a) Schematic view of sputtering process and (b) sputter deposition chamber

Figure 14 shows the sputtering mechanism and the conventional sputter deposition schematically. In the ion bombardment process, the target surface also emits secondary electrons and these electrons supply the maintenance of the plasma. Although the basic sputter deposition have been known for many years, it is limited by low ionization efficiencies and low deposition rates [28]. These limitations are overcome by the magnetron sputtering technique, where magnetic field parallel to the target is created and the target surface traps the secondary electrons in the nearby of the target. As a result the amount of ionizing electron-atom collisions increases which results in a denser plasma. Denser plasma means increased ion bombardment of the surface, which results in a higher deposition rate. Also high density plasma enables working at low operating voltages.

Magnetron sputtering can be either done by direct current (DC) or radio frequency (RF) sources. DC mode is used for conducting targets. If the target is non-conducting, and since the DC mode moves the ions in one way, the positive charges will pile up on the target surface that causes the blockage of sputtering. In the RF mode both conducting and non-conducting targets can be used.

In the semiconductor industry, the sputter deposition is used to deposit conducting and non-conducting films for various purposes. It is also used for coating the tools, corrosion resistant coating, patterning of wafer surfaces for microfabrication. Another application area of the sputter deposition is the photovoltaics. For light trapping of solar cells, antireflective coatings can be deposited by sputtering. Metal and transparent conductive oxide (TCO) films are usually deposited by magnetron sputtering. Deposition of a-Si:H for thin film silicon was investigated for Si heterojunction solar cell application, but due to the advantages of the plasma enhanced chemical vapor deposition (PECVD) technique, magnetron sputtering has not found any commercial applications. This work investigates possible reasons for the failure of the use of magnetron sputtering in this regard.

2.1.2. The Sputtering System

The sputtering system used in the a-Si:H deposition is Nano D100 magnetron sputtering system constructed by Vaksis. It has three independent magnetrons at the bottom of the vacuum chamber. Both RF and DC power supplies are present; also the sample can be rotated to obtain more uniform thin films. In Figure 15, the schematic of the sputtering system is shown.

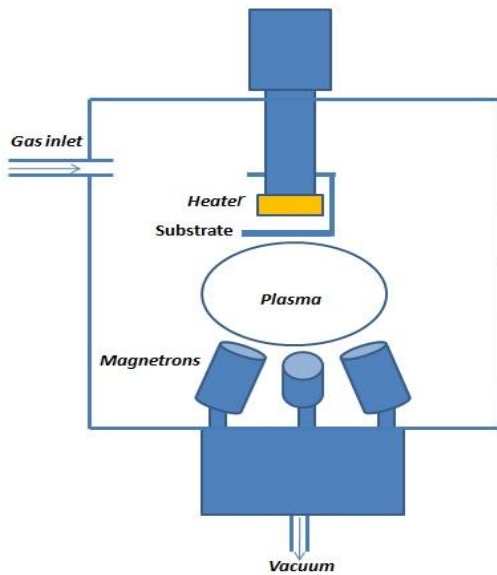


Figure 15: Schematic of the sputtering system used in this work

2.1.3. The Samples

We have fabricated a-Si thin films on p-type and n-type wafers. The sample preparation consists of the following process steps :

- i. Chemical cleaning,
- ii. Back contact formation,
- iii. a-Si:H deposition onto the front surface,
- iv. ITO deposition and front contact formation.

These process steps are described below very briefly :

Cleaning: In the sample cleaning process, ultrasonic and the so-called piranha cleaning methods are used. Firstly, wafers are ultrasonically cleaned in acetone, isopropanol and DI-water for 10 minutes in each step. The piranha cleaning follows the ultrasonic cleaning. A mixture of sulfuric acid (H_2SO_4) and hydrogen peroxide (H_2O_2) having purities of 98% and 30% are mixed with a concentration of 3:1 $H_2SO_4:H_2O_2$ for piranha process and

samples are exposed to the solution for 15 minutes and then rinsed in the DI-water. In this cleaning process, an oxide layer is formed on the surface. This oxide layer is then removed by hydrofluoric acid (HF) solution of 1:10 HF:H₂O where HF has a purity of 38%.

Back contact formation: Following the cleaning process, the sample is loaded into the evaporation chamber to deposit aluminium (Al) or silver (Ag) back contact. A 200 nm thick Al or Ag layer is formed by thermal evaporation. For ohmic contact formation, the deposited thin films are annealed at 450°C for 30 minutes.

a-Si:H deposition: Prior to a-Si:H deposition, front side of the sample is cleaned with 1:10 HF:H₂O solution to remove the native oxide formed during the annealing. p-type and n-type targets with low resistivity are used to deposit a-Si with respective conductivity type. In all samples, film thickness is in the 10-30 nm interval. Both RF and DC powers are used with different gas mixtures (Ar+H₂). During the deposition, the chamber pressure is kept constant in all experiments at 4 millibar while the substrate temperature is 200°C. The deposition rate was 1nm/min.

ITO deposition: After a-Si deposition, an indium tin oxide (ITO) layer, which is the conductive and transparent window layer, was deposited on a-Si by sputtering. In all samples ITO was deposited from ITO target at room temperature at a pressure of 5x10⁻³ Torr. A DC power of 30W was used to form a layer of 80 nm thickness approximately in 10 minutes.

Front contact formation: For the front contacts, shadow masks with finger pattern were used. The contact was formed by evaporating Ag. List of samples prepared in this work is shown in Table 2

Table 2: a-Si:H thin films prepared by magnetron sputtering

Sample	Film type	Power	Ar(sccm)	H ₂ (sccm)	T _{substrate} (°C)	Thickness(nm)
p-1	(n)a-Si:H	RF-200W	20	10	No heating	20
p-2	(n) a-Si:H	RF-200W	20	10	200	20
p-3	(n) a-Si:H	DC-100W	20	3	200	20
p-4	(n) a-Si:H	RF-200W	20	5	200	20
p-5	(n) a-Si:H	DC-50W	10	10	200	20
n-1	(p) a-Si:H	DC-50W	10	10	200	20

2.2. Fabrication of Polycrystalline Si Thin Films

2.2.1. Deposition of Thin Si Film by e-Beam Evaporation

Another PVD method of thin film fabrication is based on the thermal evaporation of the material. Simply, thermal energy is transferred to atoms in a liquid or solid phase such that their temperature is raised to the point where they can evaporate. In the deposition process, atoms are transferred from the heated source to the substrate where the film growth takes place. Thin film deposition by evaporation has been known for about 150 years [29]. However, applications have emerged in the last 50 years following the development of industrial vacuum technologies were developed [30]. Basically in the evaporation process, the target material is put in a boat or filament, generally made of tungsten, and the material is then heated by a current passing through the electrodes as shown in Figure 16. The deposition rate can be controlled by adjusting the temperature of the source through the amount of applied current to the boat or filament.

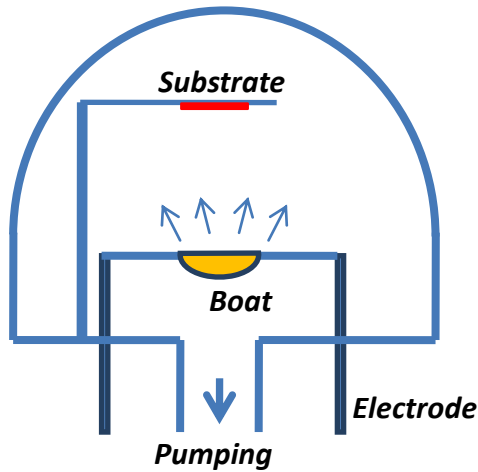


Figure 16: Schematic of a typical evaporation system

The evaporation rate can be estimated from the equation:

$$\Phi = \frac{\alpha N(P_e - P_h)}{(2\pi m R_g T)^{1/2}} \quad (7)$$

In equation (7), Φ is the evaporation rate, N is Avogadro constant, α , evaporation coefficient which is between 1 and 0, P_e , vapor pressure, P_h , the hydrostatic pressure on the source, m , the molar weight, R_g , the gas constant and T is the temperature.

Evaporation through resistive heating has the drawback of contamination from crucible and the heaters. Furthermore, working with a high input power is restricted. Electron beam (e-beam) evaporation technique overcomes these disadvantages and allows working with a wide range of source materials. In an e-beam system (Figure 17), the source material is placed in a water-cooled copper hearth. Since the heat is supplied through the e-beams, the small amount of the source becomes molten at the top of the target. Evaporation of the parts located near the crucible wall is prevented due to the cooled surface and not focused beam (directly) on that part which

eliminates the contamination coming from the crucible. So, the e-beam technique provides a better purity and enables working with a high power input.

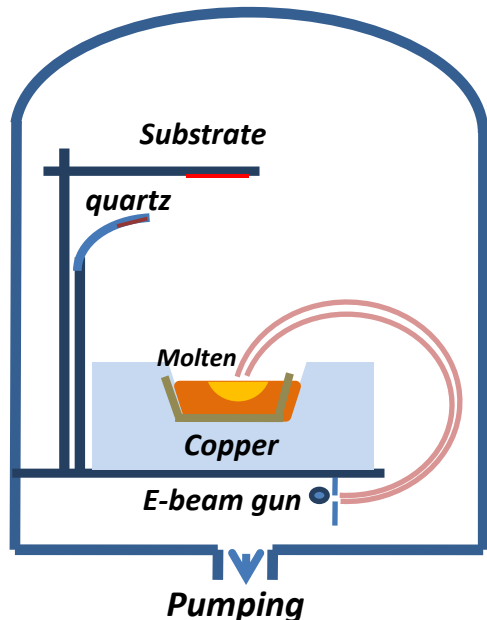


Figure 17: Schematic of E-beam evaporation System

2.2.2. The E-Beam System

The e-beam system used in thin film deposition is located at METU Physics Department. It has a single evaporation heart and supplies a maximum voltage and current of 20kV and 6mA respectively. A quartz crystal thickness monitor measuring the thickness of the film is available in the system.

2.2.3. Sample Preparation

The sample preparation was carried out in four steps:

- i. Chemical cleaning,
- ii. Boron deposition,

- iii. Silicon deposition
- iv. Annealing for crystallization.

As a substrate, silicon wafers with thermally grown SiO₂ on the surface were used. During the film growth, no substrate heating was applied.

Cleaning: In the chemical cleaning process, an ultrasonic cleaning was applied. Wafers were ultrasonically cleaned in acetone, isopropanol and DI-water for 10 minutes in each chemical and dried with N₂.

Boron deposition: To obtain a p-type silicon layer, a thin boron layer was deposited on the SiO₂ layer by evaporation from a high purity B powder (99,9999 %) . A 25 nm thick boron film was deposited on all samples at a rate of 0.7 Å/s.

Silicon deposition: Silicon deposition was obtained from high purity undoped silicon chunks. Before the deposition, the chamber was evacuated to a base pressure of 2×10^{-6} Torr. A 1 µm of Si film deposition was achieved with a deposition rate of 4-5 Å/s.

Annealing: Annealing process aims at the crystallization of the deposited Si layer and the diffusion of boron atoms into the silicon layer. In this study, a two-step annealing process was applied. In the first step, the nucleation of the crystallization was induced with an annealing at 475°C for 8 hours. In the second step, the crystallization and diffusion take place at 900°C for several minutes. At 900°C, while B diffusion was taking place, the a-Si was converted into polysilicon phase by a process called Solid phase crystallization (SPC) [31]. Table 3 shows the details of the annealing process for different samples.

Table 3: Annealing durations for the samples

Sample	475°C Annealing Time (hr)	900°C Annealing Time (min)
A	8	0
B	8	30
C	8	60
D	8	90
E	0	90

2.3. The Measurement System

I-V measurement system: For some of the samples, the dark and illuminated I-V measurements were performed by the *Keithley 2400 Sourcemeter* controlled with *Lab View* interface. Also the illuminated I-V characteristics was measured with an *Oriel AM1.5G* solar simulator, supported by *Sourcemeter* controlled by a PC software as illustrated in Figure 18.

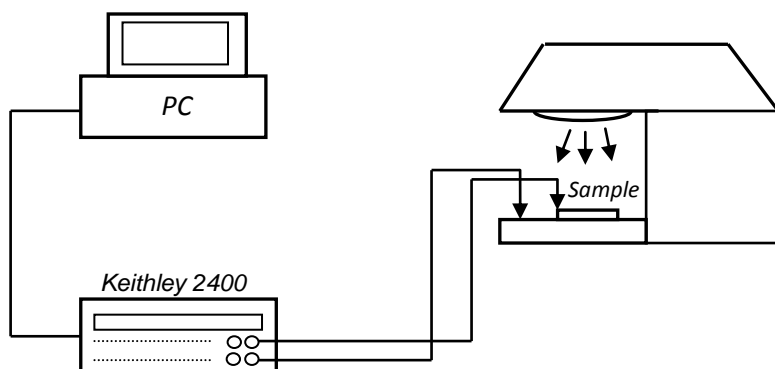


Figure 18: I-V measurement set-up

Raman System: Raman spectroscopy is an important technique for identifying the crystallinity of Si films. Basically the essence of Raman spectroscopy technique is inelastic scattering of light. In inelastic scattering,

the incoming photon interacts with the sample and the frequency of the photon is changed after reemission. Usually laser beam is used as a light source. Basically, a monochromatic light beam having a frequency ν_0 interacts with sample atoms and creates oscillating dipoles and three different frequencies are emitted from these dipoles. The scattering is called *Rayleigh scattering* if the returning light has the same frequency considering the initial light. Since there is no change in energy of photons, this is an elastic scattering. Most of the photons undergo Rayleigh scattering. If the incident photon is absorbed by Raman-active molecule, some part of the photons' energy is absorbed by Raman-active mode. As a result the frequency of the scattered light is reduced to $\nu_0 - \nu_m$, which is called *Stokes frequency*. If the frequency ν_0 is available in the excited vibrational state, extra energy is emitted as a frequency of $\nu_0 + \nu_m$ which is called Anti-Stokes frequency. Stokes and Anti-Stokes frequencies are only very little amount of emitted frequency and special measurement techniques are applied to distinguish them from the Rayleigh frequency.

In this study, Raman spectra were taken on a confocal micro-Raman, *HR800 Jobin Yvon*, attached with *Olympus* microanalysis system and a charge-coupled device (CCD) camera providing a resolution of 1 cm^{-1} . The spectra were carried out in backscattering geometry with the 632.8 nm line of He-Ne laser at room temperature.

Secondary Ion Mass Spectroscopy (SIMS): SIMS is used for compositional analysis of solid surfaces and thin films. Especially, dopant concentration and impurities are detected with a depth profile. Basically SIMS works by bombarding the sample surface by primary ions. In other words, primary ions sputter the surface. Generally primary ions like Cs^+ , O_2^+ , Ar^+ are used in SIMS. As a result many types of particles are sputtered away from the surface among these, secondary ions are separated and analyzed by a mass spectrometer.

In this work SIMS measurements were accomplished to analyze the B doping profile. SIMS measurements was carried out by *Evans Analytical Group* in United States.

X-Ray Diffraction: X-Ray diffraction gives information about the molecular and atomic arrangement in solids. In diffraction phenomena, wave is scattered from a regularly spaced obstacles having spacings comparable to the wavelength of light. The reason behind the diffraction is the phase difference between the waves that are scattered from different obstacles. This phase difference results in difference in pathlengths between scattered waves. If this path length difference is an integer multiple of the wavelength, the amplitudes are added. In other words, scattered waves constructively interfere with one another which is the condition of diffraction. If the path length difference is the integral of half wavelength, then the amplitudes cancel one another, which is destructive interference of waves. The schematic of X-Ray diffraction is given in Figure 19. The phase difference between two waves

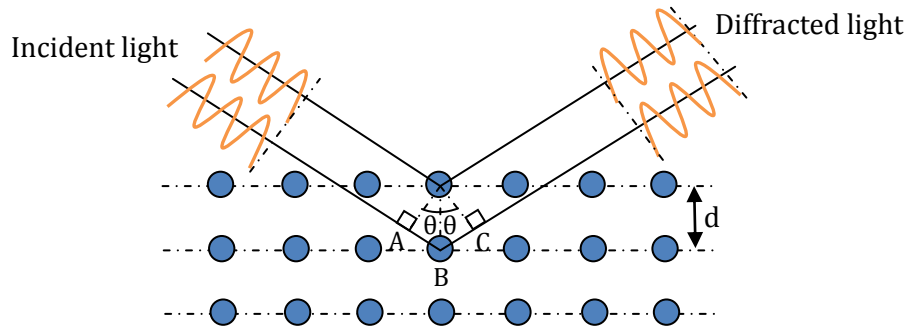


Figure 19: Schematic of X-Ray Diffraction

is the sum of the lines AB and BC. In order to accomplish constructive interference, the phase difference must be the integer multiple of the wavelength λ . This can be explained by the formula:

$$n\lambda = 2d \sin\theta \quad (8)$$

where n is the integer number, θ is the angle and d is the spacing between two planes.

X-Ray diffraction measurements were done to identify the possible crystal orientations on Si films. Measurements were carried out by X-Ray diffractometer located at METU Physics Department and X-Ray wavelength of 1.54 Å was used.

CHAPTER 3

USE OF Si THIN FILM FABRICATED BY MAGNETRON SPUTTERING FOR HETEROJUNCTION SOLAR CELL

3.1. Basic Device Structure

Heterojunction solar cells are successfully fabricated by PECVD method in which toxic gases like diborane, phosphine, and silane are used to fabricate the solar cell structure. Fabrication of thin films by magnetron sputtering is a well established technique for many applications. Magnetron sputtering is a low temperature technique which does not require any toxic gases. It is suitable for large area applications needed for solar module production. For this reason, it is worth investigating the possible use of magnetron sputtering for the fabrication of Si thin film for the heterojunction solar cells. In this chapter, we present the results on the use of thin films fabricated by magnetron sputtering.

Heterojunction solar cells are different than the thermally doped p-n junction solar cells. P-n junction formation in traditional solar cells is based on high temperature processing, which requires expensive furnace systems and a special care for the production. A similar p-n junction in silicon heterojunction (SHJ) solar cell is created by depositing a-Si:H thin film on crystalline substrate. A typical device structure and corresponding band diagram are shown in Figure 20 and Figure 21 respectively. This process is done with a relatively straight forward process at much lower temperature. Since heterostructures contain structurally different materials, bandgap profile is not like the conventional p-n junction. a-Si:H has a bandgap in the range of 1.7-2.0 eV whereas that of c-Si is 1.12 ev. When these two materials come into

contact to form a p-n junction, a band offset is created due to difference in the band energies.

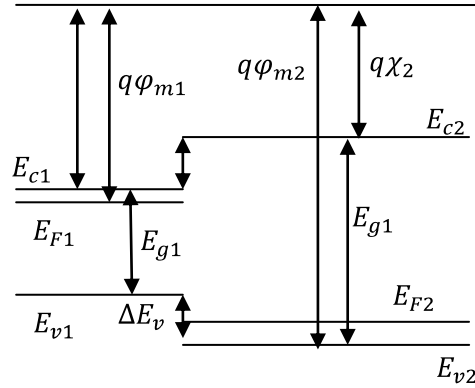


Figure 20: n-type and p-type semiconductors having different bandgaps

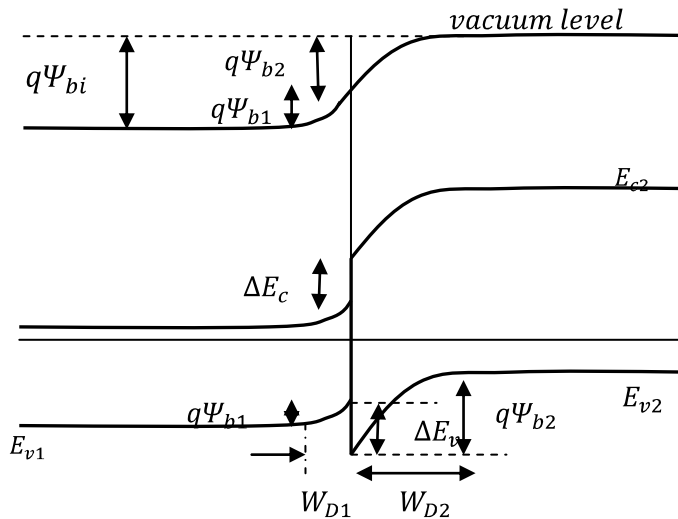


Figure 21: Band bending following contact formation of two semiconductors

In Figure 21, the band bending once the junction reaches equilibrium of an ideal (p) a-Si:H/(n) c-Si heterojunction is shown. Here two semiconductors have different bandgaps E_g , different workfunctions Φ_m and different electron affinities x . Workfunction is the energy required to remove an electron from

Fermi level E_f . ΔE_c and ΔE_v defines the energy difference between conduction and valence band edges where;

$$\Delta E_c = q(x_1 - x_2) \quad (9)$$

$$\Delta E_v = (qx_2 + E_{g2}) - (qx_1 + E_{g1}) \quad (10)$$

ΔE_c and ΔE_v depend on E_g and x , so they are unvarying also under different doping amounts. The built in potential Ψ_{bi} depends on the band bending of E_c and E_v so;

$$\Psi_{bi} = \Psi_{bi1} + \Psi_{bi2} = \varphi_{m1} - \varphi_{m2} \quad (11)$$

To understand the carrier transport in a heterojunction device, its' band structure should be understood. In case of the p-n junction device shown in Figure 21, the band offset ΔE_v formed in the valence band creates a potential barrier for the hole flow from n-type side to the p-side. Similarly, for the n-p junction shown in Figure 23, a potential barrier is formed in the conduction band for the electrons flowing from the p side to the n side. In both cases, electric field formed by the junction forces the charge carriers to move towards the contact by tunneling through these potential barriers. In heterojunctions, there are two different media which brings about two permittivities of ε_1 and ε_2 . By solving the Poisson's Equation, the depletion widths of W_{D1} and W_{D2} at both sides (Figure 22) of the junction is found as [32].

$$W_{D1} = \sqrt{\frac{2N_{A2}\varepsilon_1\varepsilon_2\Psi_{bi}}{qN_{D1}(\varepsilon_1N_{D1} + \varepsilon_2N_{A2})}} \quad (12)$$

$$W_{D2} = \sqrt{\frac{2N_{D1}\varepsilon_1\varepsilon_2\Psi_{bi}}{qN_{A2}(\varepsilon_1N_{D1} + \varepsilon_2N_{A2})}} \quad (13)$$

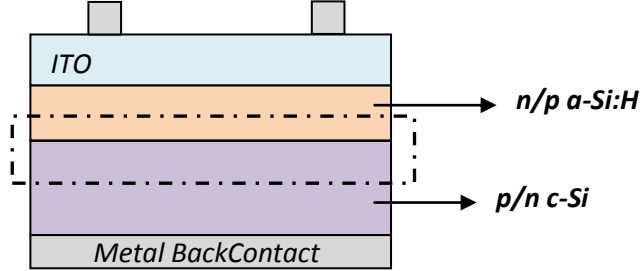


Figure 22: Depletion region on both sides of the junction

It is apparent that if there was only one media, the equations would reduce to conventional p-n junction depletion width equations;

$$W_{Dp} = \sqrt{\frac{2N_D\varepsilon_s\Psi_{bi}}{qN_A(N_D + N_A)}} \quad (14)$$

$$W_{Dn} = \sqrt{\frac{2N_A\varepsilon_s\Psi_{bi}}{qN_D(N_D + N_A)}} \quad (15)$$

The interface between the two media of the heterojunction plays a crucial role in device operation. It contains trap states due to dangling bonds and contaminations, which act as recombination centers. These recombination centers reduce the minority carrier lifetime τ . The open circuit voltage V_{oc} and short circuit current I_{sc} are influenced by τ . Besides, bulk and back surface recombination decreases V_{oc} . In Figure 23, trap states for recombinations and motion of carriers are shown in a (n)a-Si:H/(p)c-Si heterojunction.

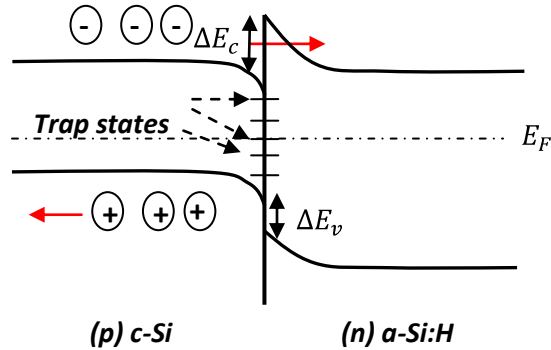


Figure 23: Trap states at the interface an electron hole motion

For an illuminated ideal diode, the net current is defined by the difference between the short circuit current I_{sc} and dark current I_{dark}

$$I = I_{sc} - I_{dark} \quad (16)$$

where;

$$I_{dark} = I_0(e^{\frac{qV}{k_b T}} - 1) \quad (17)$$

I_0 is the saturation current, q is the charge, k_b is the Boltzman constant and T is the absolute temperature. When the contacts are isolated, the voltage V becomes the open circuit voltage V_{oc} . This is the condition that I_{sc} and I_{dark} cancel each other and finally;

$$V_{oc} = \frac{k_b T}{q} \ln \left(\frac{I_{sc}}{I_0} + 1 \right) \quad (18)$$

It is clear that V_{oc} depends on saturation current. In heterostructure, it can be reasonable to write the saturation current in terms of all the saturation currents;

$$I_{total} = I_{0,bulk} + I_{0,front} + I_{0,back} \quad (19)$$

3.2. Amorphous Silicon

a-Si, having randomly arranged atomic structure is different than c-Si. Although Si atoms have covalent bonds to neighboring atoms with a tetrahedral diamond lattice structure in c-Si, it lacks long range order which is required for a crystalline structure. Some atoms may have dangling bonds which renders a-Si an unstable material. This leads to a structure in which atoms have different bonding coordinations. As shown in Figure 24, some atoms have one neighboring atom, some have three and four.

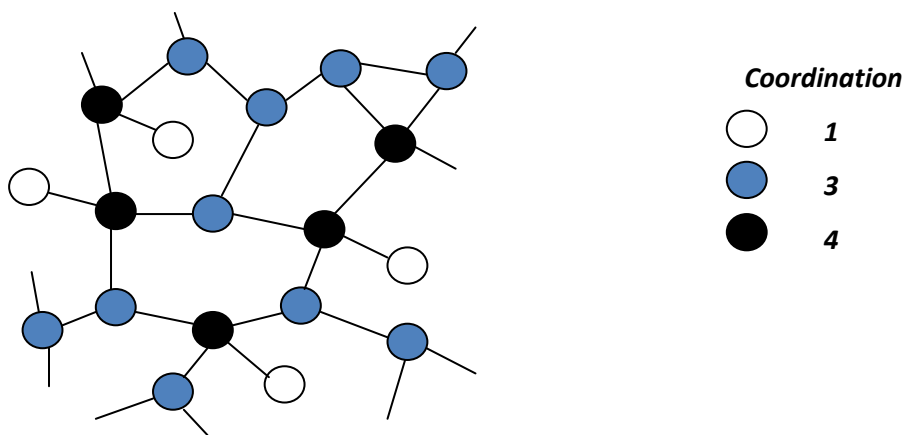


Figure 24 : Amorphous silicon structure and possible coordination of atoms

A real crystal contains defects as vacancies, interstitials and dislocations. The random structure also contains defects, but here the meaning of defect is different. In crystalline structure a point defect is the atomic irregularity in the crystal. Simplest ones are interstitials and vacancies. A defect in an amorphous structure should be related to the atomic coordination which corresponds to the presence of too many or too few bonds of an atom. The ability of the disordered network to adapt to any atomic coordination leads to an isolated coordination defect, which is not possible in a crystal structure. The disorder of an atomic structure is represented by Pair Distribution

Function (PDF) as shown in Figure 25, which is the probability of finding an atom at distance r from another atom.

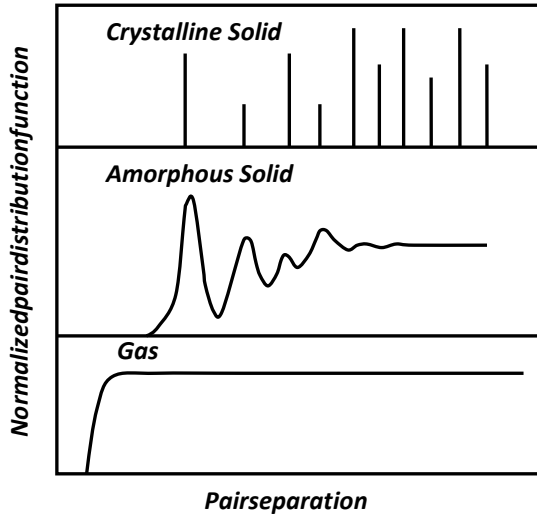


Figure 25: PDF of crystalline and amorphous solid and gas [33]

a-Si has short range order. The first few neighbours are distinguished but further increment of pair separation makes PDF approach the gas phase because after a few interatomic spacings, the structure loses the correlation between atom pairs.

In materials, the atomic structure and the sequence of atoms identify the electronic properties. Amorphous and crystalline silicon have different electronic and optical properties, because of the difference in their crystallinity. In c-Si, Bloch Theory provides an explanation of the the atomic structure. The uniform periodic potential arising from the atom cores results in bandgap formation as can be deduced from the Bloch formalism. However, in a-Si, theoretical approaches based on periodic potential is not sufficient to explain the electronic structure. The nonperiodicity of the amorphous structure modifies the density of states compared to c-Si. Major difference from the c-Si is the band tail and defect states as schematically shown in

Figure 26. The optical properties and the electronic transport are substantially affected by this modification in the band structure. Below, some description of band tail states and related topics are discussed.

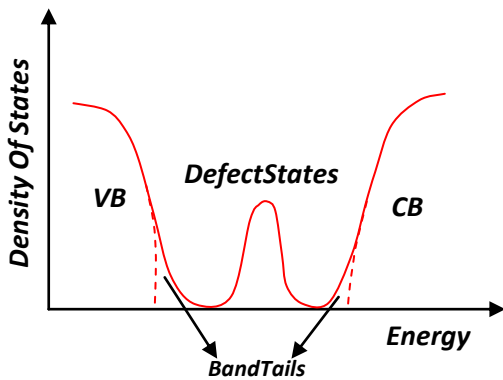


Figure 26: Density of states of amorphous silicon

Band Tails: In a-Si, the distance between atoms are not well defined due to the random orientation. The variation in the Si-Si distance and orientation gives rise to a spreading in the electron energy levels relative to c-Si. This spreading of energy appears as tail states at the bottom of conduction band (CB) and at the top of valence band (VB). This tail formed at the band edges are called Urbach Tail.

Defects: As mentioned above, atoms in a-Si have different coordination states. Dangling bonds arises from the Si atoms which are coordinated only to three neighboring Si atoms, where one valence orbital is not involved in bonding. A dangling bond may be neutral (D^0), positively (D^+) or negatively (D^-) charged. An excess of D^- states gives rise to n-type whereas excess of D^+ creates a p-type a-Si material. External effects like heating, sudden cooling, irradiating, doping can create more defects. These defects can create energy levels located in the band gap.

Hydrogenation: As-deposited a-Si is not suitable for applications since it contains too many defects. Passivation of the dangling bonds with hydrogen

decreases the defect states and creates a more stable material. As illustrated in Figure 27, the hydrogenation saturates the states in the band gap and creates a more flat density of states profile in the bandgap.

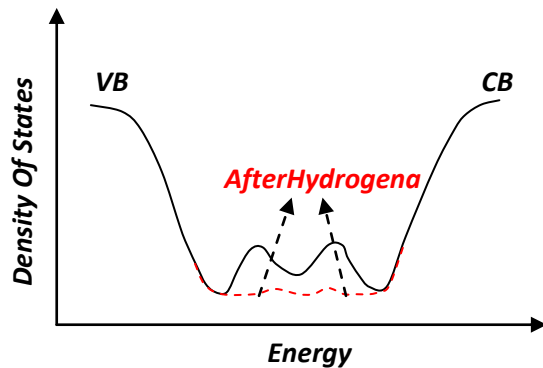


Figure 27: Effect of hydrogenation

Generally, in the solar cell terminology, the name a-Si refers to hydrogenated a-Si (a-Si:H).

3.3. SHJ Solar Cells fabricated by magnetron sputtering

In this part the dark and illuminated results of the SHJ solar cells fabricated by magnetron sputtering are given. The basics of the experimental parameters were given in Chapter 2. Before discussing the I-V results, the properties of a-Si following hydrogen passivation is given. The a-Si was deposited on glass and *UV-Visible* spectrometer was used to understand the optical properties. A wavelength range between 325 and 900 nm was used for both glass reference and film deposited glass for the UV-Visible measurements. First, the as grown sample (without hydrogen) was characterized and then the same sample annealed in a H₂ and N₂ environment at 400°C in a tube furnace for 20 minutes was studied. The Figure 28 shows the effect of hydrogenation.

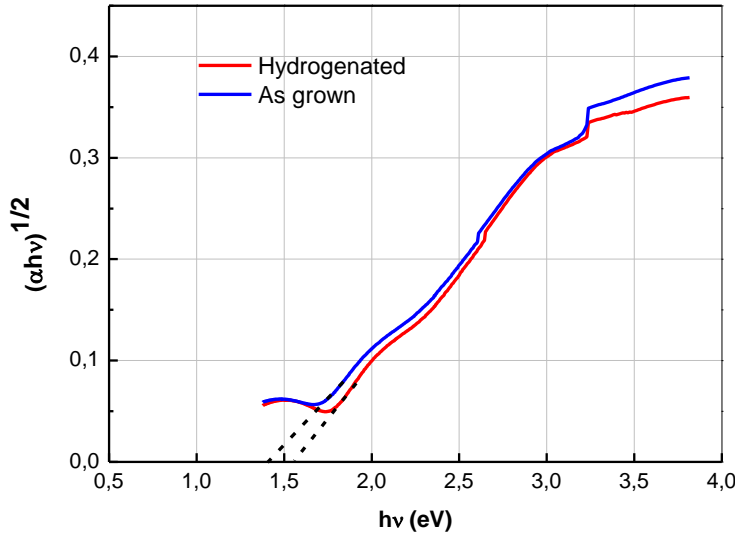


Figure 28:Tauc plot for bandgap as-grown and hydrogenated a-Si

The graphs shown in Figure 28 are called Tauc plots and are used to determine the bandgap of the fabricated amorphous thin films [34]. In a-Si, since there is no defined momentum (k) space, an electron can be excited directly to the conduction band with no need of phonon. In other words the a-Si behaves like a direct bandgap material. Tauc plot method is based on the equation:

$$\alpha h\nu = A(h\nu - E_g)^2 \quad (20)$$

where α is the absorption coefficient, $h\nu$ is the energy, A is the constant and E_g is the optical gap. In Tauc plot, bandgap is estimated by prolonging the straight part as shown in Figure 28. As it is clear from this figure, the bandgap shifted from 1.4 eV to approximately 1.6 eV. This is an obvious a result of saturation of the band gap states by hydrogen atoms.

For all samples labeled with ‘p’, the devices were fabricated on p-type (1-10 Ωcm resistivity) substrates with an amorphous layer deposited using n-type

silicon target. For the samples p-1 and p-2, the aim was to show the effect of ITO layer on carrier collection and the effect of ITO annealing on conductivity. Sample p-2 has the three versions: p-2a was fabricated without any ITO layer, sample p-2b was made on a heated substrate with ITO, and sample p-2c is the same as p-2b but annealed after ITO deposition. Annealing was done in a tube furnace under N₂ gas at 350°C for 20 minutes. All p-2 and p-1 samples have the same a-Si film deposition parameters. Summary of process parameters is shown in Table 4.

Table 4: p-1 and p-2 samples

p-1		ITO annealed	No substrate heating
p-2	p-2a	Without ITO	Substrate heating at 200°C
	p-2b	ITO not annealed	
	p-2c	ITO annealed	

Illuminated I-V measurements were done using a halogen lamp fixed to a certain height from the sample under the test. The total light power falling on the sample surface was about 30 mW/cm². Figure 29 shows the dark I-V curve of the four samples.

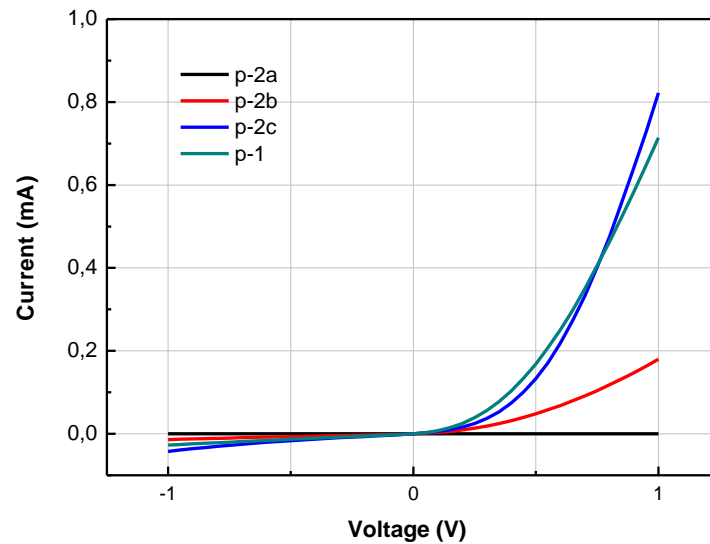


Figure 29: Dark I-V measurements of p-1 and p-2

I-V characteristics of the illuminated samples are shown in Figure 30.

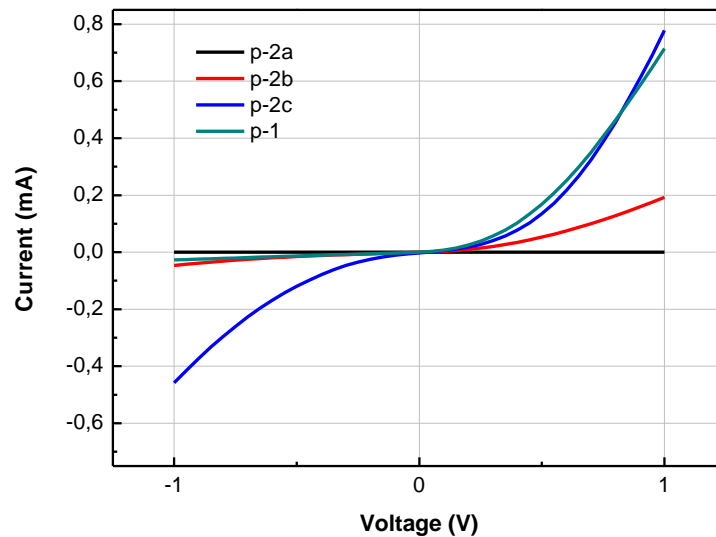


Figure 30: Illuminated I-V measurements of samples p-1 and p-2

The obtained I-V curves that are showing a typical diode behavior with a high series resistance. They exhibit more optical activity with the applied bias,

indicating that there is a potential barrier for the photo-generated carriers to surmount. The optical activity of these samples is found to be very low for the unbiased case. Here, although the optical current values are very low it is clear that ITO layer has a notable effect on carrier collection. If p-2a and p-2b are considered, the difference in current is rapidly increasing with the applied voltage for both dark and illuminated measurements. The p-1 and p-2c samples both have the same a-Si and ITO thin films. They have nearly the same I-V curve. The small difference is perhaps within the experimental fluctuation. This result shows that substrate heating has a very little effect on the result.

Even though some improvements have been observed with ITO annealing, the photo-generated current is still very low due to the reasons discussed below. In the following part the results obtained from the samples with ITO surface annealed at 350°C is discussed. A summary of this sample set is given in the Table 5

Table 5: Process parameters of samples p-3, p-4, p-5 and n-1

Sample	Film type	Power	Ar(sccm)	H ₂ (sccm)	T _{substrate} (°C)	Thickness(nm)
p-3	(n) a-Si:H	DC-100W	20	3	150	20
p-4	(n) a-Si:H	RF-200W	20	5	150	20
p-5	(n) a-Si:H	DC-50W	10	10	150	20
n-1	(p) a-Si:H	DC-50W	10	10	150	20

These samples were designed as a solar cell so that they can be characterized by the solar simulator. A picture of one of the samples with the solar cell grids used in these experiments is shown in Figure 31. This grid pattern has the thickness of approximately 200 nm and the width of the bus bar is 1 mm, width of the fingers are 0,5 mm and spacing between the fingers is 2,5 mm.



Figure 31: A picture of the sample with the solar cell grids

3.3.1. Effect of the sputter type

Samples p-3 and p-4 were fabricated with RF and DC magnetron systems separately respectively. In this experiment the aim was to understand the effect of sputtering system on the results. In a DC magnetron system, we expect the surface of the sample to be exposed to the ion beam more directly and consequently, more surface damage is created than the RF system. In order to test this effect, we run the system with the same process parameters. In both experiments, same amount of argon gas was given into the chamber. However, in the DC power regime, the amount of hydrogen is lower because, depending of the requirements of plasma sustainability. In Figure 32 the dark and illuminated I-V measurements of samples p-3 and p-4 are given.

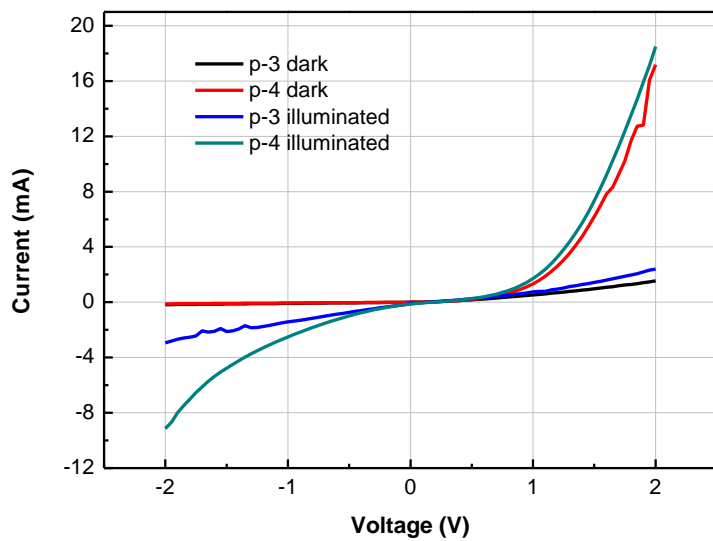


Figure 32: Dark and illuminated I-V measurements of samples p-3 and p-4

It is seen from these figures that the sample produced with RF magnetron system generates higher photocurrent at high voltage. It seems that the voltage barrier is somewhat lowered in this case. This might be related to the increased resistivity due to the damages created by the DC accelerated ions during the sputtering. Solar simulator results of samples p-3 and p-4 are shown in Figure 33. Both the open circuit voltage (V_{oc}) and the short circuit current (I_{sc}) are much lower than what we would expect for a solar cell. We see from Figure 33 that, although it is almost insignificant, RF sputtering yielded slightly better open circuit voltage, possibly due to its less damaged surface.

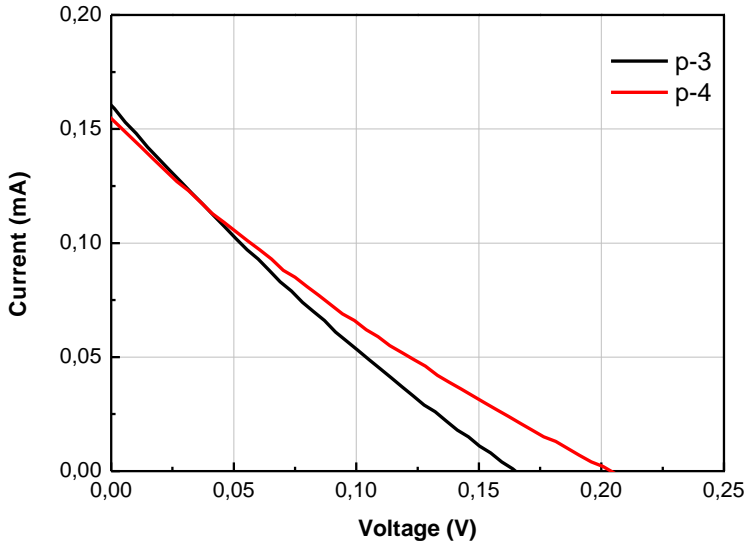


Figure 33: Solar simulator I-V measurement of p-3 and p-4

3.3.2. Effect of sputtering power

The effect of sputtering power on the device performance was also investigated. The aim was to see if the power reduction has any positive effect on decreasing the interface states which would improve the device performance. In the high power deposition process, the surface is exposed to highly energetic ions which may damage the surface and increase the defect density [35]. The DC power is decreased to 50 W for the sample p-5 and a solar cell is fabricated. Another advantage of decreasing DC power is that the sputtering system enables more hydrogen to be incorporated into the film. Figure 34 shows comparison of the dark and illuminated I-V results of sample p-5.

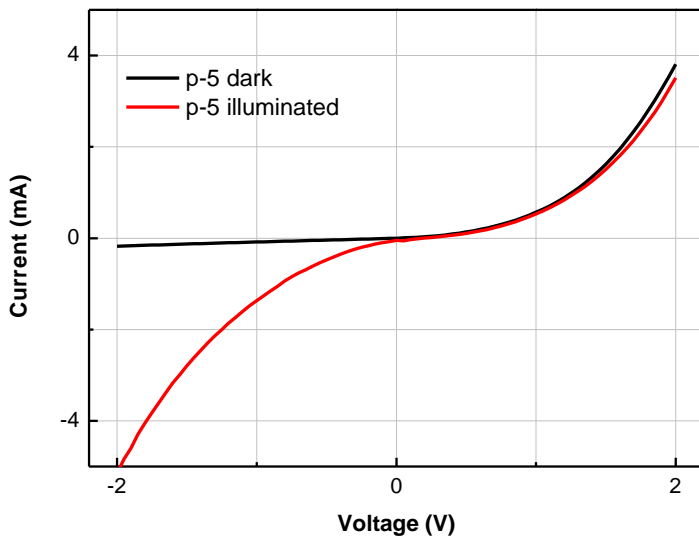


Figure 34: Dark and illuminated results of sample p-5

It is clear in Figure 34 that there is no significant change between dark and illuminated results on the positive bias region. The solar simulator I-V measurement is given in Figure 36. p-5 has lower open circuit voltage and short circuit current.

3.3.3. Effect of substrate type

In order to see if the substrate type has any significant effect on the solar cell performance, the same device structure on the n-type substrate was fabricated. We used the same process parameters with the previous sample was used. It is known that highest efficiency SHJ solar cell has the n-type base [36]. However, no significant improvement in the device performance was observed. In Figure 35, dark and illuminated I-V measurements of the sample n-1 is shown to be almost similar to what we measured from the p-type samples. The results obtained from the solar simulator are shown in Figure 36 in comparison with the sample p-5. It is observed that fabrication of the solar cell on n-type substrate did not generate any better result.

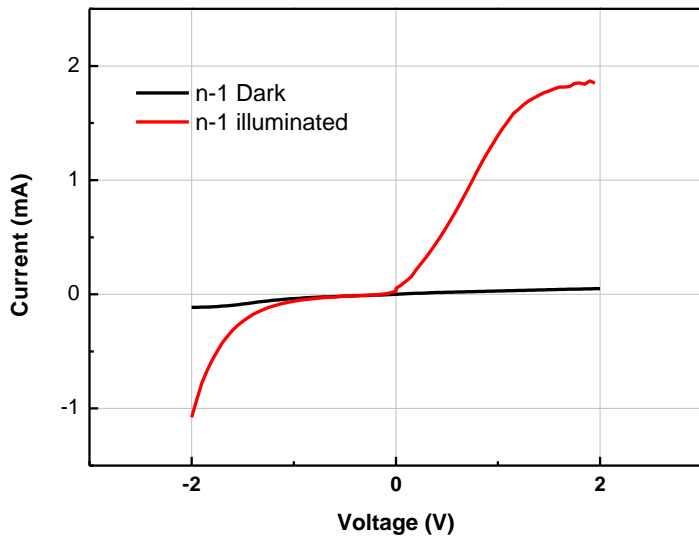


Figure 35: Dark and illuminated results of sample n-1

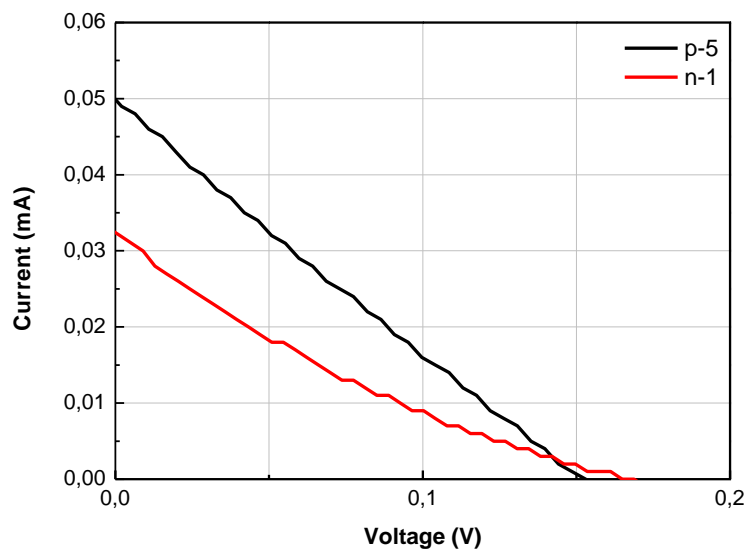


Figure 36: Solar Simulator results of samples n-1 and p-5

3.4. Discussion on the use of Si thin film fabricated by magnetron sputtering

Table 6 summarizes the results that we have obtained from the solar cells fabricated by magnetron sputtering. We see that the results are far from the desired solar cell characteristics.

Table 6: Solar cell characteristics of the samples

	$V_{oc}(V)$	$I_{sc} (mA)$	$FF(%)$	Efficiency (%)
p-3	0,164	0,160	22,034	0,006
p-4	0,203	0,155	20,776	0,007
p-5	0,151	0,050	23,989	0,002
n-1	0,167	0,032	18,348	0,0009

There may be two reasons for this low efficiency values. The first reason is related to the low charge collection from the Si substrate. The obtained I-V curves are analyzed and it is found that a significant photo current is generated upon the application of a voltage. This means that carriers are generated but not collected at zero bias condition. This is indicating that we have not been able to form the necessary band profile needed to collect the generated carrier. In another words, generated carriers are not directed towards the external contacts for collection. The schematic potential profile is shown in Figure 37 and Figure 38 corresponding to the ideal heterojunction band profile, and the band structure possibly occurring in our case respectively. The band profile shown in Figure 37 possibly resulted from the problems of doping with magnetron sputtering. It was expected that using a heavily doped n-type Si target would be sufficient to obtain n-type Si thin film. This was indeed reported in the literature before [35]. In order to understand if the deposited thin film is doped or not, resistivity measurements were carried out. 200 nm of a-Si:H films were deposited on glass substrates by

using the same Si target and approximately 200 nm of metal was evaporated through a mask for electrical contacts. The mask used has bars of length 0,5 cm and width 2 mm. spacing between the bars is 0,5 cm. We have obtained a resistivity value in the order of 10^4 - 10^5 Ωcm . Table 7 shows some resistance and resistivity values of a-Si:H deposited by different sputtering types. It is clear that the resistivity values are very high, indicating that the deposited layers are not properly doped.

Table 7: Some example resistance values

	H ₂ (sccm)	R (Ω)	ρ (Ωcm)
200W RF	10	$1,01 \times 10^{10}$	$2,02 \times 10^5$
150W DC	3	$1,37 \times 10^9$	$2,74 \times 10^4$

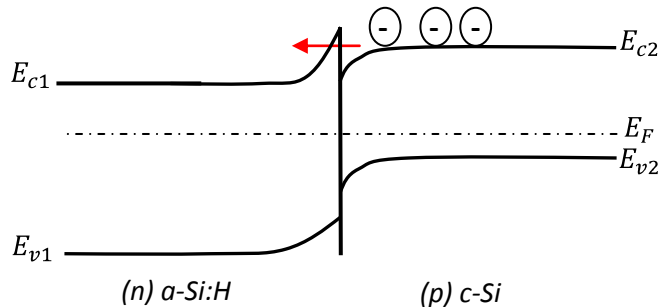


Figure 37: Ideal heterojunction band diagram

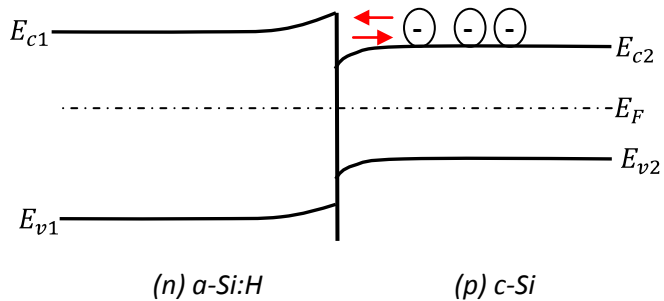


Figure 38: Heterojunction with impeded carrier motion

Resistivity values indicate that, contrary to the expectations, the deposited films are not sufficiently doped. It is then possible to claim that we have not formed any p-n junction at the surface. The lack of the p-n junction at the surface causes the undesirable band profile formation shown in Figure 38.

The second reason for the low efficiency is again related to the doping of the deposited layer. The high resistivity in the deposited a-Si:H layer creates very high series resistance in the device. This high series resistance causes significant loss in the current flow even if the charges are generated and collected by the heterojunction.

We conclude that doping is a crucial problem in the thin films deposited by magnetron sputtering. A standard sputtering process does allow an easy doping for the deposited films. Using a highly doped target does not necessarily produce n doped thin films. This problem should be solved for successful device applications. One solution would be to deposit p-type layer by thermal evaporation during the sputtering. This can be accomplished using a special deposition technique in which both thermal evaporation and sputtering are combined.

CHAPTER 4

POLYCRYSTALLINE SILICON THIN FILMS AND SOLAR CELL APPLICATIONS

4.1. Electronic Properties of Polycrystalline Materials and Electronic Transport

Polycrystalline materials are composed of crystalline regions separated by boundaries. These regions are called grains and boundaries are called grain boundaries. Every grain has its' own crystal orientation. Grain sizes vary from a few nm up to cm. In general, the properties of polycrystalline materials are dominated by the grain boundaries. They prevent the propagation of dislocations that may cause plastic deformation. They also form an obstacle for the charge carrier transport. In this case, the grain boundaries act like a barrier as trap states for electrons and holes. In polycrystalline silicon thin films, grain sizes are much lower than the bulk polycrystalline material. For this reason, the carrier transport is more limited in thin films than bulk materials. Figure 39 shows a schematic of polycrystal silicon.

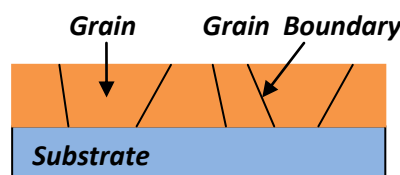


Figure 39: Schematic of polycrystalline silicon film

Thin film polycrystalline silicon, especially those used in solar cell applications, have very large surface/volume ratio. In these systems, the

surface structure affects the carrier transport and have a more prominent effect than bulk materials. If the mean free path of the carriers are comparable to the film thickness, surface scattering can dominate the electrical properties of the film. The surface passivation is then an important issue for the devices made of thin film polycrystalline materials.

The carrier mobility in a material is determined through taking into account different scattering mechanisms like impurity scattering and phonon scattering. In the thin film polycrystalline materials, in addition, the possible scattering mechanisms are, *specular reflection* where the carriers' velocity component perpendicular to the surface is only reversed after scattering and there is no change in momentum, the scattering is elastic, as a result there is no contribution to conductivity and *diffuse reflection* where the velocity changes with respect to the incident one and the scattering is random, so change in the energy of the carrier affects the conductivity

Since the grain boundaries are the edges of the crystalline regions, they contain dangling bonds and defects. These dangling bonds and defects constitute energy states within the bandgap of polysilicon [37] and located near the midgap behave as the recombination centers for the free carriers moving in the conduction and valence bands. Strained bonds conceive the tail states near the conduction and valence band edges like in a-Si (Figure 40).

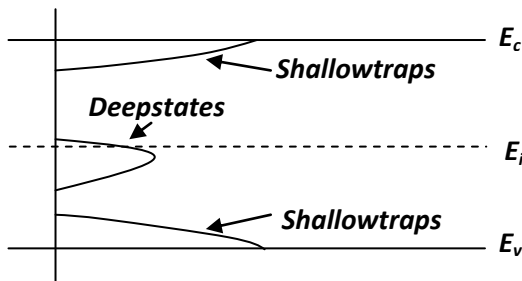


Figure 40: The effect of dangling bonds and defects

Another important effect of grain boundaries is the segregation of the dopant content. The substitutional dopant atoms segregate [38] at the boundaries since they act as energetically favourable places for them. Dopant atoms residing at the grain boundaries lose their electrical properties. Like dopant atoms, free carriers can also be trapped at the grain boundaries. The amount of trapping is enhanced by substitutional dopant atom segregation to the grain boundaries [39]. These free carriers create an extra charge at the grain boundaries and depletion regions are formed around the boundaries. The curvature due to the depletion regions causes potential barriers that inhibits the movement of majority carriers between the grains [39].

The electronic structure at the grain boundaries and carrier transport through them can be understood by solving the Poisson's equation;

$$\frac{d^2V}{dx^2} = \frac{qN}{\varepsilon} \quad (21)$$

where N is the dopant concentration at the grain boundaries, x_d is the width of depletion region, q is the charge, ε is the permittivity, the barrier height can be inferred as;

$$V_B = \frac{qN}{2\varepsilon} x_d^2 \quad (22)$$

The dopant concentration has a notable effect on potential barriers. The total number of trapped carriers per unit area at the grain boundaries is less than the number of traps N_T at low dopant concentrations. In this case, the depletion regions extend through the grains and the potential barrier qV_B is small which is shown in Figure 41 for a p-type polycrystalline silicon. As a

result, free carriers can move between the grains. If the dopant concentration increases, the number of carriers that are trapped at the grain boundaries will

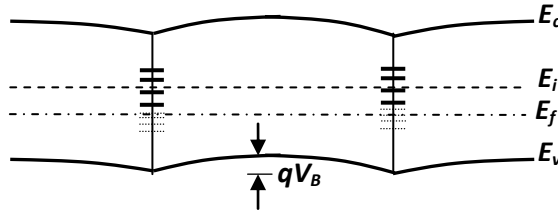


Figure 41: Polycrystalline silicon with low dopant concentration

increase with the potential barriers will increase. This makes the transport of carriers more difficult (Figure 42).

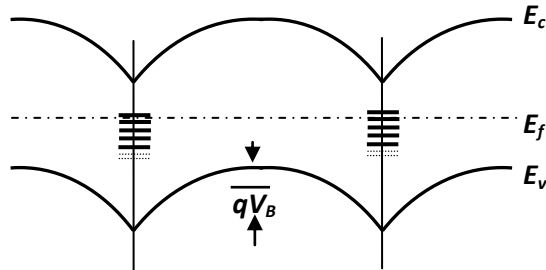


Figure 42: Polycrystalline silicon with increased dopant concentration

Like the dopant concentration, the amount of trap states are very important for the potential profile at the interface. For relatively low trap concentration or very high dopant concentration, trap states are usually completely filled and neutralized so that extra carriers are not trapped by the grain boundaries anymore (Figure 43).

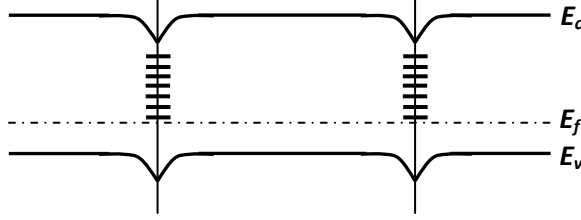


Figure 43:Polycrystalline silicon following the filling of trap states

Futhermore, the barriers start to decrease after this threshold value. In this regime, depletion region can be defined by:

$$X_D = \frac{N_T}{2N} \quad (23)$$

and the barrier height from equation (22):

$$V_B = \frac{qN}{2\varepsilon} \left(\frac{N_T}{2N} \right)^2 \quad (24)$$

In solar cell applications, minority carrier transport is crucially important to achieve high efficiency values. However, due to the trapped majority carriers at the grain boundaries, the minority carriers recombine with them. This renders the lifetime τ_{eff} of minority carriers low when compared to the crystalline structures. The minority carrier lifetime can be expressed as [40]:

$$\tau_{eff} = \frac{2d \exp(-\frac{qV_B}{KT})}{3\sigma v D_T(E_{fn} - E_{fp})} \quad (25)$$

V_B is the height of the potential barrier, D_T is the interface trap density and E_{fn} , E_{fp} are the quasi-Fermi levels. It states that both the barrier height and grain size have an important effect of the carrier life time.

4.2. Polycrystalline Silicon Thin Films: Fabrication and Characterization

Polycrystalline silicon thin film formation starts with the deposition of a-Si. a-Si is e-beam evaporated and has no hydrogen content. Details of e-beam evaporation system and deposition were given in Chapter 2. Following the deposition of a-Si layer with a thickness of 1 μm , the samples were annealed at 475°C and 900°C for the polysilicon formation. In order to fabricate a p-type graded region, 25nm of boron film was deposited before a-Si deposition. In Figure 44 schematic view of the sample before and after annealing is shown.

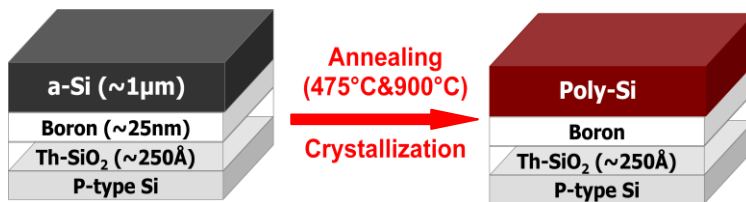


Figure 44: Schematic view of the sample before and after annealing

A two-stage annealing process was performed in this work in order to investigate the effect of crystallization procedure on the crystallinity and the grain size of the Si layer. This process consists of annealing at 475°C and 900°C for different durations as described below:

Annealing at 475°C: For all samples, annealing at 475°C was performed for 8 hours. It is expected that no crystallization occurs at this temperature, except some nucleations in a-Si films. In crystallization process, it is known that the nucleation sites start to form before the crystallization. At higher temperatures, the number of nucleation sites is high, and for this reason, the resultant grain sizes are small. It is expected that the number of nucleation

sites will be lower at 475°C, and this will result in larger grain sizes after the consequent growth process at higher temperature.

Annealing at 900°C: is the second step of annealing to complete the growth process. Following annealing at 475°C, some samples are exposed to this annealing step for 30, 60 and 90 minutes for the comparison. The aim of this part is not only the crystallization but also the diffusion of B atoms. The boron film under the Si layer diffuses into the Si and creates a B graded region.

4.2.1. Raman Analysis

In the analysis of polysilicon films, Raman spectroscopy is a quite important technique to study the crystallinity of the grown structure. The crystalline silicon has the characteristic Raman peak at wavenumber of 521cm^{-1} . Crystal structure of the polysilicon films was identified with respect to this peak of c-Si. Firstly, in order to see the effect of first step annealing, Raman measurements were carried out after 8 hours annealing at 475°C . In Figure 45 the Raman result of sample A is given. For comparison, spectrum taken from Si crystal is also shown. It is clear from this figure that the Raman signal measured from the annealed sample is peaked around 480 cm^{-1} , which is well below the crystalline Si peak at 521 cm^{-1} . We also know that the Raman peak of a-Si is located at around 480 cm^{-1} and the Raman peak is usually very broad due to the amorphous nature of the material.

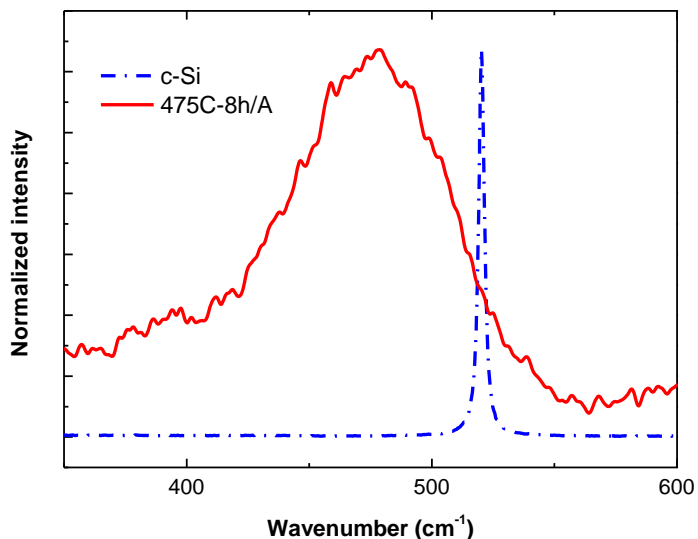


Figure 45: Raman spectra of sample A, annealed at only at 475°C/8h

Depending on the observations and clear reference data available in the literature, it is concluded that the film annealed at 475°C is still in the amorphous phase. This confirms that there is no crystallization annealing at this stage. The Raman signal obtained from the sample which is further annealed at 900°C/30min, sample B, after the low temperature annealing is shown in Figure 46.

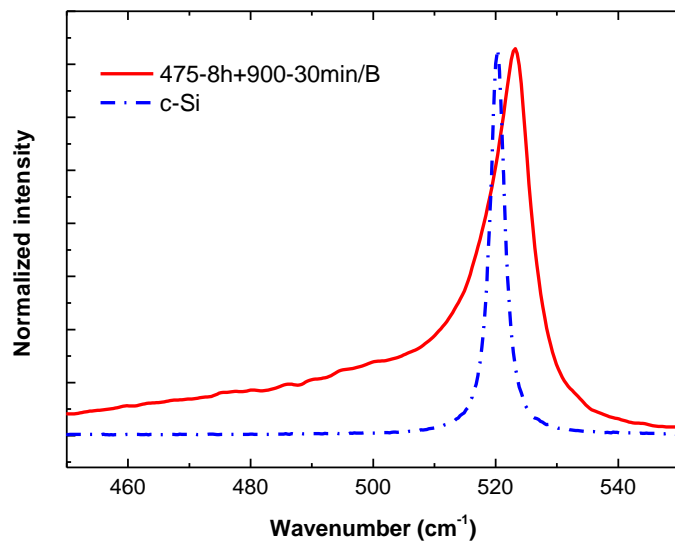


Figure 46: Raman spectra of sample B

It is clear from this figure that, the annealing at 900°C shifts the Raman peak to the crystalline regime. The full width half maximum (FWHM) of the Raman signal becomes smaller and approaches that of the reference c-Si. However, the tail seen on the left side of the main peak indicates that there is still some material with the amorphous phase. In another experiment, annealing time was increased to 60 min and 90 min to see if the crystallinity was improved in this way. The result obtained from sample C and D is shown in Figure 47.

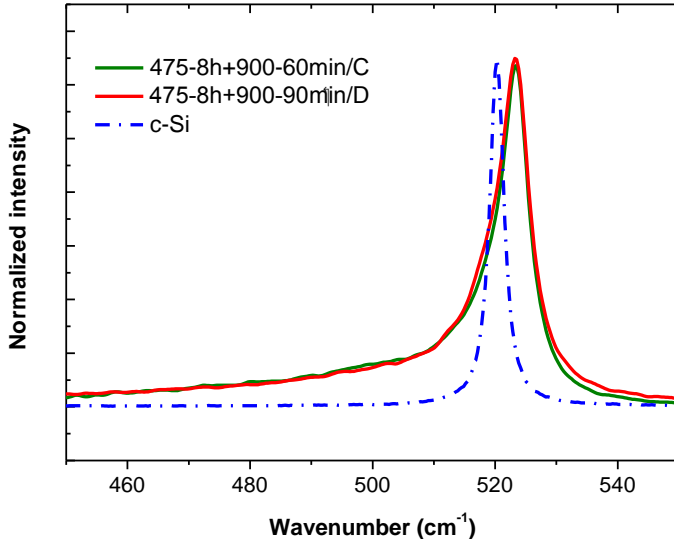


Figure 47: Raman spectra of sample C and D

Raman measurement of sample C has a narrower peak shape compared to sample B, indicating that it has a higher crystalline fraction. However, there is no noticeable difference between sample C and sample D in terms of peak position and peak width. It can be concluded that no more significant crystallization takes place after 60 minute annealing. In Figure 48, sample E which is only annealed at 900°C for 90 minutes is compared with sample D. From the major peak located at around 523 cm⁻¹, no notable difference in crystallinity is observed. However, if the Raman peak at 150 cm⁻¹ is investigated, shown in Figure 49, slightly a different picture appears. The peak seen at 150 cm⁻¹ is attributed to the intermediate range disorder in a-Si with some crystallinity [41]. As stated in Ref [42], the intensity of this signal decreases with disorder. When the Raman results shown in Figure 49 is compared, it is observed that a-Si has the maximum signal intensity in agreement with the above statement about the intermediate range disorder. The intensity of the signal obtained from the single step annealing at 900°C generated a signal lower than the a-Si layer. The minimum signal intensity was obtained from the sample annealed in two steps. This is showing that the grain size is the largest in two step annealed sample (sample D) as expected.

However, this conclusion is based only on the small difference in the noisy Raman signal obtained at very low wavenumbers. Therefore, this needs to be confirmed by electron backscatter diffraction (EBSD) measurements.

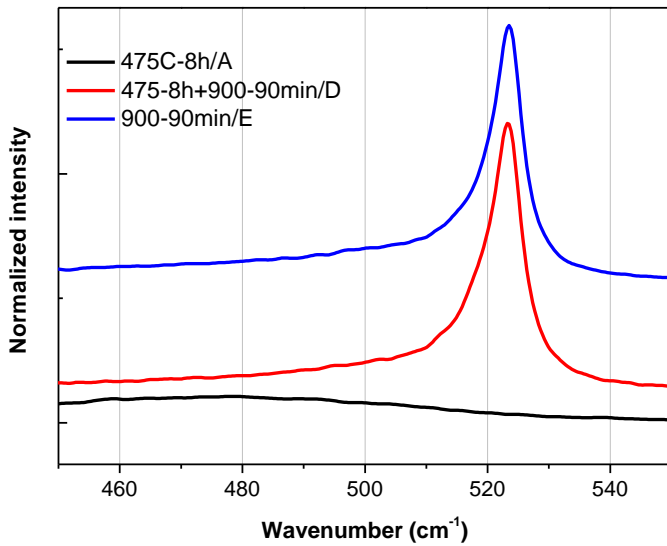


Figure 48: Raman spectra of samples D, E and A

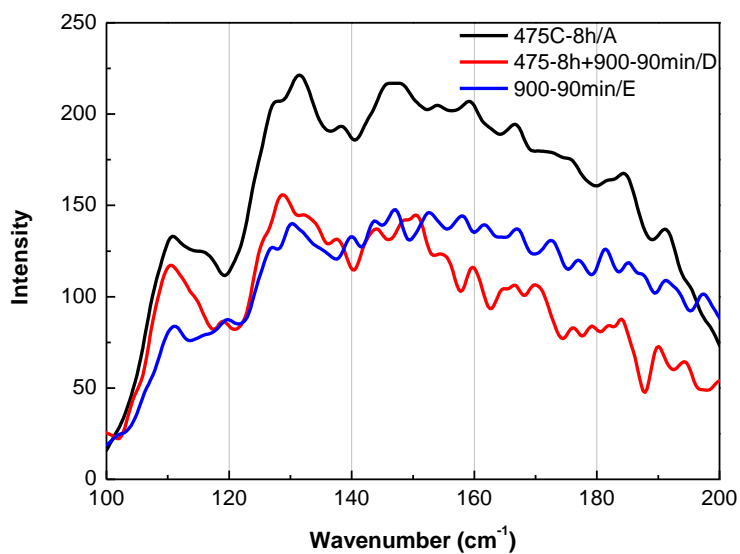


Figure 49: Raman spectra of samples A, D and E at low wavenumbers

The overall crystallinity of the film can be determined from the Raman peaks through the analysis of the peaks corresponding to amorphous and crystalline peaks. For this purpose, different signals comprising the observed main peak at 523 cm^{-1} should be resolved by a deconvolution process. We used the software program called Peak Fit to obtain the peaks shown in Figure 50. Following this deconvolution process, the amount of crystallization can be calculated by the following expression [42]:

$$X_{RC} = \frac{I_2 + I_3}{I_1 + I_2 + I_3} \quad (26)$$

Table 8: Crystalline fractions of the samples obtained from Raman measurements

	Sample B	Sample C	Sample D	Sample E
% X_{RC}	91	93	93	95
Peak Position	523,21	523,19	523,33	523,46
FWHM	8,96	6,51	7,33	6,52

where I_1, I_2, I_3 are the integrated Raman intensities corresponding to the amorphous phase, intermediate phase and the crystalline phase, respectively. The results are shown in Table 8 for different samples. The peak position and FWHM values are also shown for comparison. It is apparent that the samples have very similar values for the crystallinity. However, it is clear that this analysis is insufficient to resolve the grain sizes. Again for the grain size analysis, an EBSD analysis is necessary.

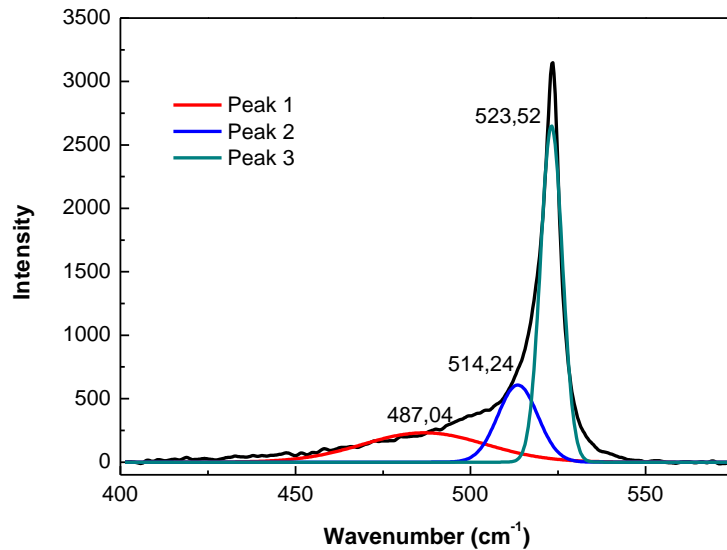


Figure 50: Peak Fit analysis for Sample C

4.2.2. XRD Results

Since the Si film becomes polycrystalline after the growth, there should be different orientations of grains that could be observed by XRD. After the Raman measurements, X-Ray diffraction measurements were performed on all samples that we fabricated. In all of the samples the substrate was thermally grown SiO₂ on <100> oriented wafer, so in x-ray measurements the highest intensity comes from <100> c-Si substrate at about 68 degrees. In sample A, in agreement with the Raman measurements, no XRD peak is observed. Again, there is no indication for the crystallinity in this sample (Figure 51).

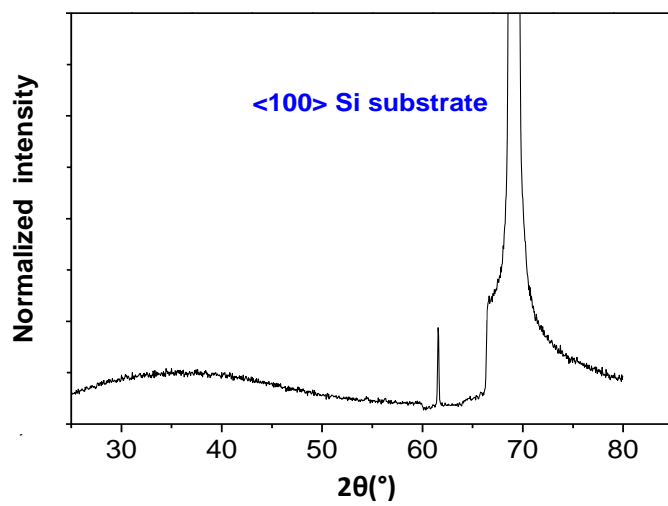


Figure 51: X-Ray diffraction spectra of sample A

A broad XRD signal peaked around 35° results from the a-Si. Samples annealed at 900°C give XRD signals originating from the c-Si. The broad a-Si peak disappeared in these samples after high temperature annealing (Figure 52-54).

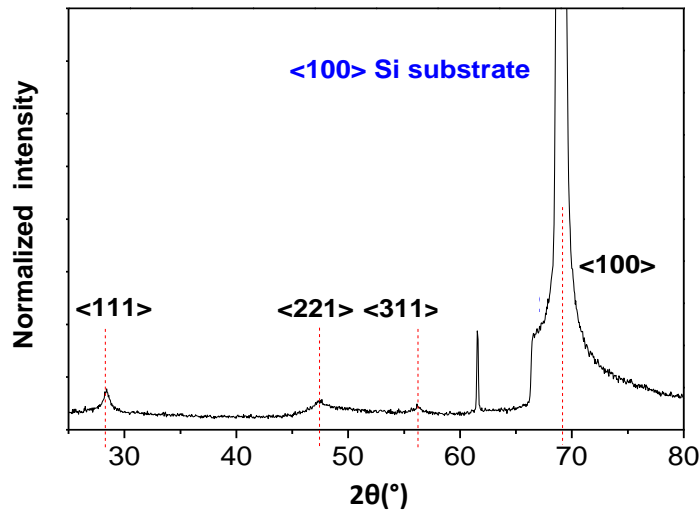


Figure 52: X-Ray diffraction spectra of sample B

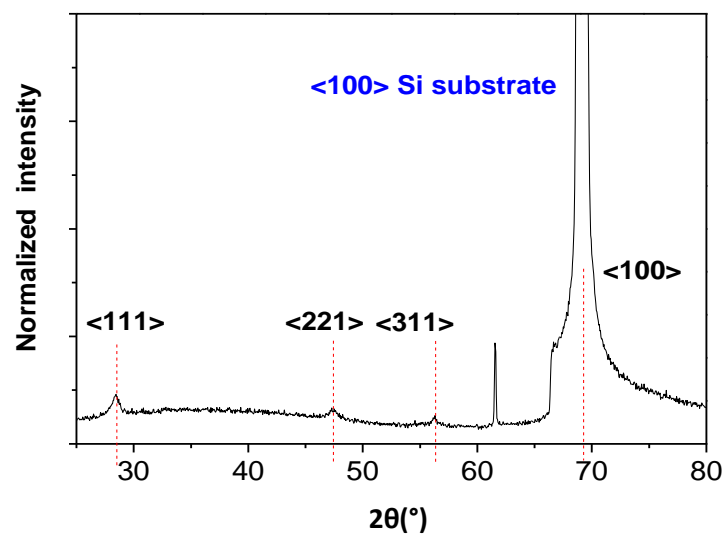


Figure 53: X-Ray diffraction spectra of sample C

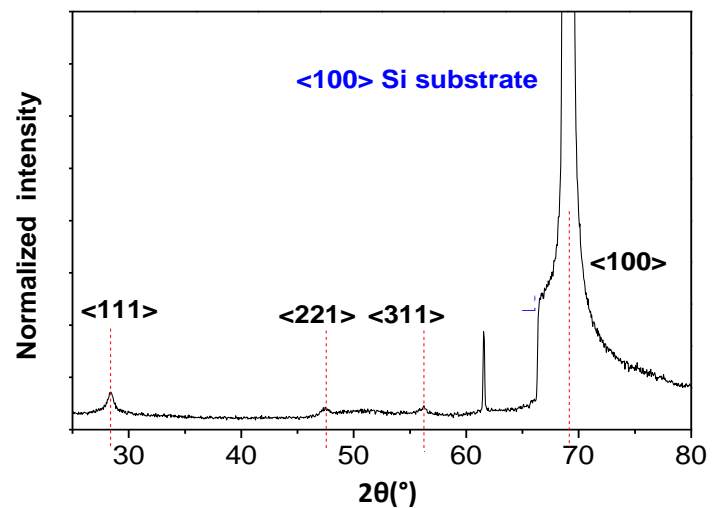


Figure 54: X-Ray diffraction spectra of sample D

Boron distribution is determined by the Secondary Ion Mass Spectrometry (SIMS). Boron doping is crucially important for the device applications. For this purpose, a thin layer of B layer was evaporated under the poly-Si layer as described before. The B profile was determined by SIMS measurements

and displayed in Figure 55-56. Graded B distribution has been obtained in both cases. There is no significant variation in the B distribution after the when the annealing time was increased from 60 min. to 90 min.

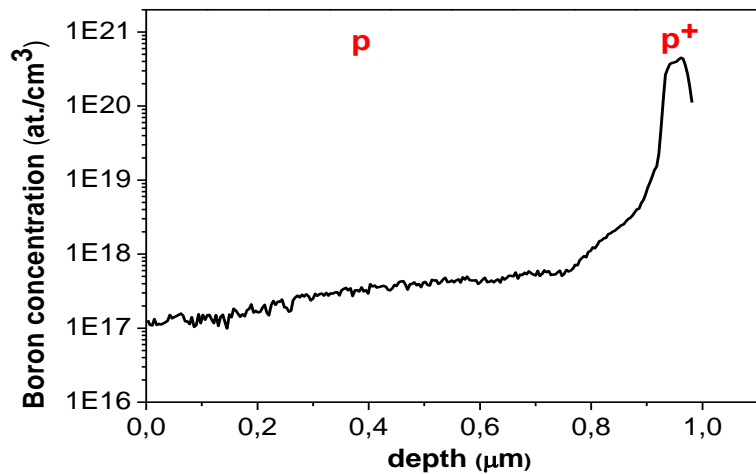


Figure 55: SIMS profile of sample C

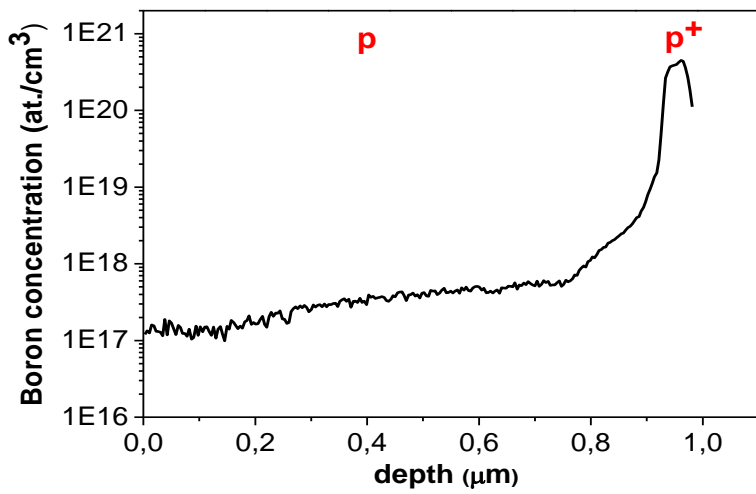


Figure 56: SIMS profile of sample D

In both samples the B profile is approximately same. Since B diffuses into Si, a graded structure from p⁺ to p is created. At the bottom of the film, there is nearly 200 nm of highly doped region

CHAPTER 5

CONCLUSIONS

In this thesis, fabrication and characterization of Si thin films using magnetron sputtering and e-beam evaporation towards the fabrication of heterojunction solar cells and thin film c-Si solar cells on glass substrates were investigated. These two methods of thin film fabrication are not used in the today's conventional solar cell technology, which employs PECVD as the major thin film fabrication method. However, PECVD suffers from the high temperature requirements and extreme toxicity of the gases used for the fabrication. On the other hand, both the magnetron sputtering and the e-beam evaporation offer low temperature operation in a non-toxic environment. They also provide flexibility in the growth rate which is critically important for the cost of the thin film systems. These advantages make them very attractive for the photovoltaic applications. This study attempted to understand the properties of the these thin film system for such applications

In the first part of this work, the magnetron sputtering technique was employed for the Si thin film deposition. Thin film samples were prepared both in the form of simple material structure or in the form of solar cell device structure. The material properties such as resistance and optical transmittance were determined. First of all, it was found that the deposited films have amorphous structure with a band gap of around 1.4 eV in agreement with commonly observed value for a-Si. It was observed that the hydrogen content of the films is important for the band gap of the deposited film. When the fabricated film was annealed under hydrogen atmosphere the band gap increased to 1.6 eV. This is due to the saturation of tail states in the band gap of a-Si.

For the device realization, the effect of ITO layer on the properties of the device in the form of a simple solar cell was studied. It was observed that application of ITO as the contact layer improves the device performance. Both dark and illuminated I-V characteristics were improved upon application of ITO film on the surface of the device. This is expected because it was observed that the a-Si layer is extremely resistive and a large area contact is needed to reduce the overall resistance of the system. Further improvements were obtained with the annealing of ITO layer after the deposition.

The heterojunction solar cells (SHJ) fabricated using a-Si layers deposited by magnetron sputtering have exhibited unsatisfactory performance. Although superior devices were not expected by this technique, the device performance has been surprisingly low. In order to overcome the problems and improve the device performance, some experiments were carried out to test the effect of the process types and parameters. The effects of the type of the magnetrons, namely, RF and DC were studied. It was observed that the sample produced with DC magnetron system generates more photocurrent at high voltage values. It seems that the voltage barrier is somewhat lowered in this case. This is understandable because the DC magnetron causes more damage on the surface which lowers the specific resistance at the interface. Moreover, dark and illuminated measurements showed that the sample deposited by RF power collects more photocurrent than the sample deposited by DC power. The less defective interface in the sample fabricated by RF results in better solar cell performance as expected.

Finally the dependence of the device on substrate type by making the device on the n-type substrates was investigated. No significant improvement on the device performance was observed with n-type substrate.

From the series of experiments summarized above, about the device properties the following conclusions were reached:

After the I-V results are analyzed a significant photo current was generated when a voltage is applied to the system. This means that carriers are generated but not collected at zero bias condition. This is a result of undesired band profile across the device, which does not direct the generated carriers towards the external contacts for collection. This result, along with the measured low resistivity, leads us to the conclusion that the deposited a-Si layer is not properly doped. Although we used heavily doped n-type target material for the sputtering, the resultant material is not n-type doped, meaning that no p-n junction is formed at the interface.

The other very important reason for the low efficiency is again related to the doping of the deposited layer. The high resistivity in the deposited a-Si layer creates very high series resistance in the device. This high series resistance causes significant loss in the current flow even if the charges are generated and collected by the heterojunction.

It can be concluded that doping is a crucial problem in the thin films deposited by magnetron sputtering. A standard sputtering process does not allow straightforward doping for the deposited films. Using a highly doped target does not necessarily produce n-type doped thin films. This problem should be solved for the fabrication of a decent device.

In the second part of this thesis work, the fabrication of crystalline Si thin film on SiO_2 substrate using e-beam evaporation was studied. c-Si wafer based solar cells have the drawback of having high thicknesses about 200 μm which causes high material consumption for the solar cell production. For the absorption of the light, only a few μm is enough and the rest of the wafer is unnecessary. It is then of a great interest to fabricate c-Si thin films on a cheap substrates like glass or metal foils. In this study, we fabricated thin film polysilicon on SiO_2 layer thermally grown on crystalline Si. SiO_2 substrate provides a glass like substrate.

For the thin film polysilicon fabrication, e-beam evaporation system at METU Physics Department was used. Like in the case magnetron sputtering, we need to obtain a proper doping in the deposited films. For this purpose,a pure boron film was first deposited onto SiO₂ layer before the Si deposition. The technique of Solid Phase Crystallization (SPC) was applied to achieve polysilicon structure. In this study, a two-step annealing process was compared with the single step annealing. The first step of the annealing was done at 475°C for 8 hours and the second step was done at 900 °C for different durations. The aim of the two-step annealing was to minimize the number of nucleation sites in this way and achieve larger grain sizes. Raman measurements showed no crystallization after the first step annealing. The second step of annealing at 900°C induced the crystallization as expected. We studied the effect of annealing duration on the crystallinity of the layer and found that the crystallinity increases with the annealing duration up to certain time after which no significant variation is observed.

XRD measurements also confirmed that the sample annealed at 475°C only has an amorphous structure and the crystallization occurs after the high temperature annealing at 900°C. From the XRD data we observed that the preferred orientation is <111> for solid phase crystallized films.

The structural analysis based on XRD and Raman indicated that the SPC process is clearly achieved after the 900°C annealing. Upon comparison of the Raman signals, we found some indications for the larger grain sizes in the two-step annealed sample. The Raman signal at 150 cm⁻¹ is a function of long range disorder. We observed that this signal is reduced in the two-step annealed sample compared to the single step annealed one. This indicated that long range disorder is reduced in this sample probably due to the larger grain sizes.

Finally, SIMS measurements were carried out to determine the boron distribution in the deposited film. We found that B incorporation has been

achieved successfully from pure B layer deposited under the poly Si layer. The diffusion of the B atoms during the annealing creates a graded profile for the device operation.

However, in order to obtain conclusive results on the grain sizes, Electron Back Scattered Diffraction (EBSD) experiments should be performed. Besides this, the appropriate device can be completed by n-type doping. This can be achieved by spin-on technique which is an easy method of doping. These experiments have been planned as a future work.

BIBLIOGRAPHY

- [1] “*Time For Change*” Web, <http://timeforchange.org/prediction-of-energy-consumption>, last accessed on 10/08/2010
- [2] “*Light sensitive device*” U.S. Patent 2,402,662, 25/06/1946
- [3] “*The Silicon Solar Cell Turns 50*” Perlin, John (2004). National Renewable Energy Laboratory. Retrieved 5 October 2010.
- [4] “*Global solar installations forecast for 2010*” Web.
http://www.pvtech.org/news/isuppli_bets_big_on_global_solar_installations_forecast_for_2010_reaching_1, last accessed on 20/04/2010
- [5] “*Growth of Thin Film Microcrystalline Silicon Solar Cells*” M.S. Thesis. Oyediran David Oludare, Delft University of Technology 2009
- [6] Green M. “*Solar Cells: Operating Principles, Technology, and System Applications*” Chap. 1, Prentice Hall, Englewood Cliffs, NJ, 1–12 (1982).
- [7] “*PVCDROM*” Web. <http://pveducation.org/pvcdrom/properties-of-sunlight/atmospheric-effects>, last accessed on 18/07/2011
- [8] Gueymard, C. Solar Energy, Volume 76, Issue 4, April 2004, Pages 423-453.
- [9] Star Solar “*Difference between monocrystalline polycrystalline and Amorphous thin film solar cell*” Web. <http://www.pvsolarchina.com/difference-between-monocrystalline-polycrystalline-and-amorphous-thin-film-solar-cell.html>, last accessed on 14/08/2011
- [10] “*EU PVSEC: Neo Solar Power launches monocrystalline solar cell with 19% efficiency*” Web. <http://www.elektor.com/news/monocrystalline-solar-cells-achieve-19-efficiency.917704.lynkx>, last accesed on 05/09/2011

- [11] J. Meier, J. Sitznagel, U. Kroll, C. Bucher, S. Fay, T. Moriarty, A. Shah, Thin Solid Films 451–452 (2004) 518
- [12] A.V. Shah, J. Meier, E. Vallat-Sauvain, N. Wyrsch, U. Kroll, C. Droz, U. Graf Solar Energy Materials and Solar Cells 469-491, (2003)
- [13] Martin A. Green, Keith Emery, Yoshihiro Hishikawa, Wilhelm Warta, Prog. Photovolt: Res. Appl. 2011; 19:84–92
- [14] O. Kunz, Z. Ouyang, S. Varlamov, A. G. Aberlez. Prog. Photovolt: Res. Appl. 2009; 17:567–573
- [15] O. Kunz, Z. Ouyang, J. Wong, A. G. Aberle. Volume 2008, Article ID 532351
- [16] T. Matsuyama, N. Terada, T. Baba, T. Sawada, S. Tsuge, K. Wakisaka, S. Tsuda, J. Non-Cryst. Solids 198–200 (1996) 940.
- [17] J.J. Ji, Z. Shi, US patent 6420647 (2002).
- [18] P.A. Basore, Proc. 21st European Photovoltaic Solar Energy Conf., Dresden, 2006, WIP, Munich, 2006, p. 544.
- [19] P.A. Basore, Proc. 19th European Photovoltaic Solar Energy Conf., Paris, 2004, WIP, Munich, 2004, p. 455.
- [20] P.I. Widenborg, A.G. Aberle, Advances in OptoElectronics, vol. 2007, 2007, doi:10.1155/2007/24584,
- [21] R. Grigorovici, R. Croitoru, N. Marina, I. Natasi. Rev. Roumaine Phys., vol.13 (1968), 317
- [22] W. Fuhs, K. Niemann and J. Stuke, Proc. Internat. Conf. Tedrahedrally Bonded Amorphous Semiconductors, Yorktown (1974), p.345
- [23] W. E. Spear, P. G. Le Comber. Solid State Communication, vol.17 (1975), 1193

- [24] K. Okuda, H. Okamoto and Y. Hamakawa, *Jpn. J. Appl. Phys.*, vol.22 (1983), L605
- [25] T.Takahama, M.Taguchi, S.Kuroda, T.Matsuyama, M.Tanaka, S.Tsuda, S.Nakano and Y.Kuwano, Proc. of the 11 th European Photovoltaic Solar Energy Conference, Montreux (1992), pp.1057-1060
- [26] H. Kanno, D. Ide, Y. Tsunomura, S. Taira, T. Baba, Y. Yoshimine, M. Taguchi, T. Kinoshita, H. Sakata, E. Maruyama, Proc. of the 123rd European Photovoltaic Solar Energy Conference, Valencia (2008), pp.1136-1139
- [27] K. Seshan “*Handbook of Thin-Film Deposition Processes and Techniques; Principles, Methods, Equipment and Applications*” William Andrew Publishing, Chp. 8, p. 319
- [28] R.D. Arnett, P.J. Kelly. Surface and Coatings Technology 112 (1999) 170–176
- [29] M.Faraday, *Phil. Trans.* 147, 145 (1857)
- [30] L. Holland, *Vacuum Deposition of Thin Films*, Chapman and Hall, London, 1957.
- [31] Ö. Tüzün, “*Polycrystalline Silicon Films by Aluminium Induced Crystallization and Epitaxy: Synthesis, Characterizations and Solar Cells*” Phd. Thesis p. 40 (2009)
- [32] S. M. Sze, “*Physics of Semiconductor Devices*” Wiley, Chp. 2 p.226
- [33] R.A. Street, “*Hydrogenated Amorphous Silicon*” Cambridge University Press, Chp. 1, p.5
- [34] Stenzel, O. “*The Physics of Thin Film Optical Spectra: An Introduction*” Springer. p. 214 (2005)
- [35] B. Jagannathan , W.A. Anderson, J. Coleman, *Solar Energy Materials and Solar Cells* 46 (1997) 289-310

- [36] Cousins PJ, Smith DD, Luan HC, Manning J, Dennis TD, Waldhauer A, Wilson KE, Harley G, Mulligan GP. Photovoltaic Specialists Conference (PVSC), 35th IEEE 275-278 (2010)
- [37] T. Kamins, “*Polycrystalline Silicon for Integrated Circuits and Displays*” p.201
- [38] M. E. Crowder, T. O. Sedgewick, *J. Electrochem. Soc.* 119, 1565 (1972)
- [39] T. Kamins, *J. Appl. Phys.* 42, 4357-4365 (1971)
- [40] H. C. Card, E. Yang, *IEEE Trans. Electron Devices*, ED-24, 397-402 (1977)
- [41] LIAO NaiMan, *Sci China Ser E-Tech Sci*, vol. 52, no. 2, 339-343 (2009)
- [42] Zhi Li, Wei Li, *J. Raman Spectrosc.* 2011, 42, 415–421